

Lab on a Chip

Accepted Manuscript



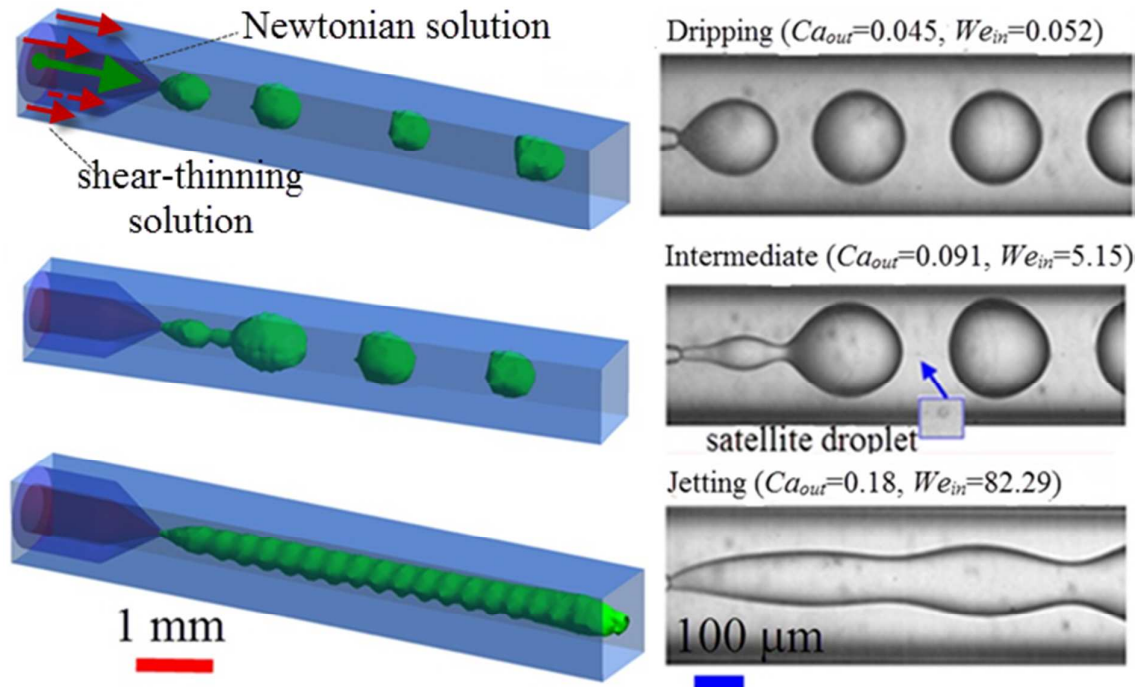
This is an *Accepted Manuscript*, which has been through the Royal Society of Chemistry peer review process and has been accepted for publication.

Accepted Manuscripts are published online shortly after acceptance, before technical editing, formatting and proof reading. Using this free service, authors can make their results available to the community, in citable form, before we publish the edited article. We will replace this *Accepted Manuscript* with the edited and formatted *Advance Article* as soon as it is available.

You can find more information about *Accepted Manuscripts* in the [Information for Authors](#).

Please note that technical editing may introduce minor changes to the text and/or graphics, which may alter content. The journal's standard [Terms & Conditions](#) and the [Ethical guidelines](#) still apply. In no event shall the Royal Society of Chemistry be held responsible for any errors or omissions in this *Accepted Manuscript* or any consequences arising from the use of any information it contains.

The shear-dependence of the viscosity of shear-thinning fluids changes the dynamics of jet breakup, necessitating new approaches for its control.



1 **Breakup dynamics and dripping-to-jetting transition**
2 **in a Newtonian/shear-thinning multiphase**
3 **microsystem**

4 Yong Ren^{*abc}, Zhou Liu^{ab} and Ho Cheung Shum^{*ab}

5 ^a *HKU-Shenzhen Institute of Research and Innovation (HKU-SIRI), Shenzhen, Guangdong,*
6 *China.*

7 ^b *Department of Mechanical Engineering, The University of Hong Kong, Pokfulam Road,*
8 *Hong Kong.*

9 ^c *Current Address: Department of Mechanical, Materials & Manufacturing Engineering, The*
10 *University of Nottingham, Ningbo, China.*

11 **Author to whom correspondence should be addressed. E-mail: yong.ren@nottingham.edu.cn;*
12 *ashum@hku.hk; Tel: +852 2859 7904*

13 The breakup dynamics in non-Newtonian multiphase microsystems are associated with a variety
14 of industrial applications such as food production and biomedical engineering. In this study, we
15 numerically and experimentally characterize the dripping-to-jetting transition under various flow
16 conditions in a Newtonian/shear-thinning multiphase microsystem. Our work can help to predict
17 the formation of undesirable satellite droplet, which is one of the challenges in dispensing non-
18 Newtonian fluids. We also demonstrate the variations in breakup dynamics between shear-
19 thinning and Newtonian fluids under the same flow conditions. For shear-thinning fluids, droplet
20 size increases when the Capillary number is smaller than a critical value, while decreases when
21 Capillary number is beyond the critical value. The variations highlight the importance of
22 rheological effects in flows with a non-Newtonian fluid. The viscosity of shear-thinning fluids
23 significantly affects the control over droplet size, therefore necessitating the manipulation of the
24 shear rate through adjusting the flow rate and the dimension of the nozzle. Consequently, the
25 droplet size can be tuned in controlled manner. Our findings can guide the design of novel
26 microdevices for generating droplets of shear-thinning fluids with predetermined droplet size.

27 This enhances the ability to fabricate functional particles using an emulsion-templated approach.
28 Moreover, elastic effects are also investigated experimentally using a model shear-thinning fluid
29 that also exhibits elastic behaviors: droplets are increasingly deformed with increasing elasticity
30 of the continuous phase. The overall understanding in the model multiphase microsystem will
31 facilitate the use of a droplet-based approach for non-Newtonian multiphase applications ranging
32 from energy to biomedical sciences.

33 **1. Introduction**

34 Microfluidic multiphase system can be applied in a wide variety of applications. For example, it
35 can facilitate drug encapsulation and release using emulsion droplets as a template to fabricate
36 core-shell microspheres, capsules and other functional materials.¹⁻³The system can also be used
37 for the generation of jets, which can work as precursors of microfibers for application in wound
38 dressing and tissue engineering.^{2,4-7}Nevertheless, the practical microfluidic multiphase
39 applications increasingly demand the use of fluids with more complex rheological behaviors,
40 such as non-Newtonian fluids, whose viscosities change with the applied stress. Non-Newtonian
41 fluids are ubiquitous in daily life; examples include blood, lotions, creams, shampoos and
42 toothpaste. They are also widely used in industrial applications such as inkjet printing, spraying
43 and coating.⁸⁻⁹Microscaled non-Newtonian multiphase systems have been increasingly applied in
44 biomedical engineering, food production, and energy applications. For instance, an electrokinetic
45 microdevice has been developed to convert fluidic mechanical energy to electrical energy by
46 means of electrokinetic phenomena such as streaming currents.⁹By reducing the hydrodynamic
47 conductance while maintaining the same streaming current, addition of an appropriate polymer

48 to the working fluid in a microchannel can enhance the energy conversion efficiency, which is a
49 ratio of electrical output power and hydrodynamic input power.¹⁰⁻¹¹

50 Non-Newtonian multiphase microsystem has become a subject of intense research, and it is of
51 paramount importance to understand the relevant physical phenomena, one of which involves the
52 deformation of liquid threads and subsequently droplet formation. The performance of the
53 droplets is intimately tied to the ability to control droplet size, which has a strong impact on the
54 droplet stability as well as optical and mechanical properties.¹²For example, when the droplets
55 are used as a template to fabricate micro/nano particles for the drug delivery system, the shape
56 and size of emulsion droplets have significant impacts on the drug release kinetics.¹³⁻
57 ¹⁴Monodisperse droplets with precisely controlled sizes can be used to deliver an accurate dosing
58 of contained payload such as drug, flavoring, or chemical reactants.¹⁵Therefore, monodispersity
59 and size tenability are highly desired for ensuring that the droplets exhibit constant, controlled
60 and predictable behaviors.^{4,12}However, the complex rheological properties of non-Newtonian
61 fluids challenge the versatility in droplet size control. For example, the stretching and/or thinning
62 of non-Newtonian liquid filaments will lead to the formation of “bead-on-string” patterns.¹⁶⁻
63 ¹⁷These beads can subsequently become undesirable satellite droplets, increasing the
64 polydispersity of the resultant droplet population. The dynamics of the droplet formation process
65 can be characterized into a dripping and a jetting regime. The dripping-to-jetting transition can
66 be estimated using the Capillary number of the continuous phase, Ca_{out} , a ratio of viscous force
67 to surface tension, and the Weber number of the dispersed phase, We_{in} , a ratio of inertial force to
68 surface tension.¹⁸

69

$$We_{in} = \frac{\rho_{DP} dV_{DP}^2}{\sigma} \quad (1)$$

$$Ca_{out} = \frac{\eta_{CP,0} V_{CP}}{\sigma} \quad (2)$$

71 where ρ_{DP} is the density of dispersed phase, d refers to the diameter of the orifice, V_{DP} and V_{CP}
72 are the velocities of dispersed and continuous phase respectively, σ is the interfacial tension, and
73 $\eta_{CP,0}$ is the apparent viscosity of the non-Newtonian fluid of continuous phase. The subscript “0”
74 refers to zero-shear rate when a shear-dependent fluid is used. Droplet formation occurs at the
75 orifice directly after the two fluids meet in the dripping process, when both Ca_{out} and We_{in} are
76 small, as surface tension dominates. By contrast, jetting occurs when Ca_{out} or We_{in} is large, as the
77 viscous stress or the inertial force on the droplet will be large enough to overcome surface
78 tension. Droplets are generated after breakup of a jet at some distance downstream in this regime.
79 While the dynamics of droplet breakup has been systematically investigated in Newtonian
80 fluids,¹⁷⁻¹⁸ the validity of the understanding has not been adequately confirmed in non-
81 Newtonian fluid systems. In addition, a number of non-Newtonian fluids such as polymeric
82 solutions, whole blood or protein solutions with large polymeric molecules often exhibit elastic
83 property due to the stretching and coiling of the polymer chains. The resultant non-Newtonian
84 rheological behaviors inspire interesting applications.¹⁹ For instance, microparticles driven in
85 viscoelastic solutions can migrate toward the centerline of a microchannel because of the first
86 normal stress difference between the centerline and the walls; three-dimensional (3D) particle
87 focusing can be achieved via a combination of inertial and elastic forces.²⁰ The elasticity of the
88 focusing fluid has been shown to facilitate formation of smaller droplets.²¹ These examples attest
89 to the need for a comprehensive understanding of the role of elastic fluids with shear-rate-
90 dependent viscosity in droplet formation using microfluidic systems.

91 In this paper, we focus on a shear-thinning fluid, which is one of the most frequently
92 encountered non-Newtonian fluids,²² and investigate the dripping-to-jetting transition of a
93 Newtonian/shear-thinning two-phase system and characterize the formation of satellite drops in
94 the model system. The breakup time and droplet size are compared with Newtonian/Newtonian
95 two-phase system at the same Weber number and Capillary number. We demonstrate that the
96 degree of control over droplet size can be enhanced by adjusting the flow rate and nozzle size,
97 thus tuning the shear rate experienced by the non-Newtonian fluids. We also present an
98 experimental study of the elasticity effect of a shear-thinning fluid on droplet generation in a
99 microfluidic two-phase system. The shape of the droplets is shown to vary with the Weissenberg
100 number, which represents a ratio of the relaxation time to the hydrodynamic time. Our work
101 helps to elucidate the effects of rheological behaviors on the breakup dynamics in a
102 Newtonian/non-Newtonian two-phase microscaled flow; our understanding inspires new
103 approaches to control sizes and shapes of functional droplets in applications requiring the use of
104 non-Newtonian fluids.

105 **2. Numerical model**

106 The microcapillary co-flow device has been widely used in emulsion generation.²³ A 3D
107 numerical model with the same design is established in the present investigation (see Fig.1a). A
108 Newtonian fluid is injected in a cylindrical capillary as the dispersed phase at a constant average
109 velocity V_{DP} . This inner fluid is surrounded by a non-Newtonian outer phase, which is injected
110 through the coaxial square capillary as the continuous phase at a constant average velocity V_{CP} .
111 The cross section (perpendicular to the main flow direction) consists of a circle inside a square
112 (see inset of Fig.1a). Thus, the continuous phase is flowing through a cross section between an

113 inner circle and outer square. No-slip condition is applied at the solid boundaries of the walls of
 114 capillaries. Gauge pressure of zero is applied at the outlet of the domain. The maximum entrance
 115 length is 9.4 μm in our numerical computations, and the length of the computational domain is 6
 116 mm, which is long enough to ensure that the fluid flow can be fully developed. The governing
 117 equations for incompressible two-phase fluids are,²⁴

$$118 \quad \frac{\partial \alpha_{CP}}{\partial t} + V \cdot \nabla \alpha_{CP} = 0 \quad (3)$$

$$119 \quad \frac{\partial \rho}{\partial t} + \nabla \cdot (\rho V) = 0 \quad (4)$$

$$120 \quad \frac{\partial}{\partial t}(\rho V) + \nabla \cdot (\rho V V) = -\nabla P + \nabla \cdot [\eta(\nabla V + \nabla V^T)] + \frac{\rho \sigma \nabla \alpha_{CP}}{\frac{1}{2}(\rho_{DP} + \rho_{CP})} \nabla \cdot \frac{\nabla \alpha_{CP}}{|\nabla \alpha_{CP}|} \quad (5)$$

$$121 \quad \rho = \alpha_{CP} \rho_{CP} + (1 - \alpha_{CP}) \rho_{DP} \quad (6)$$

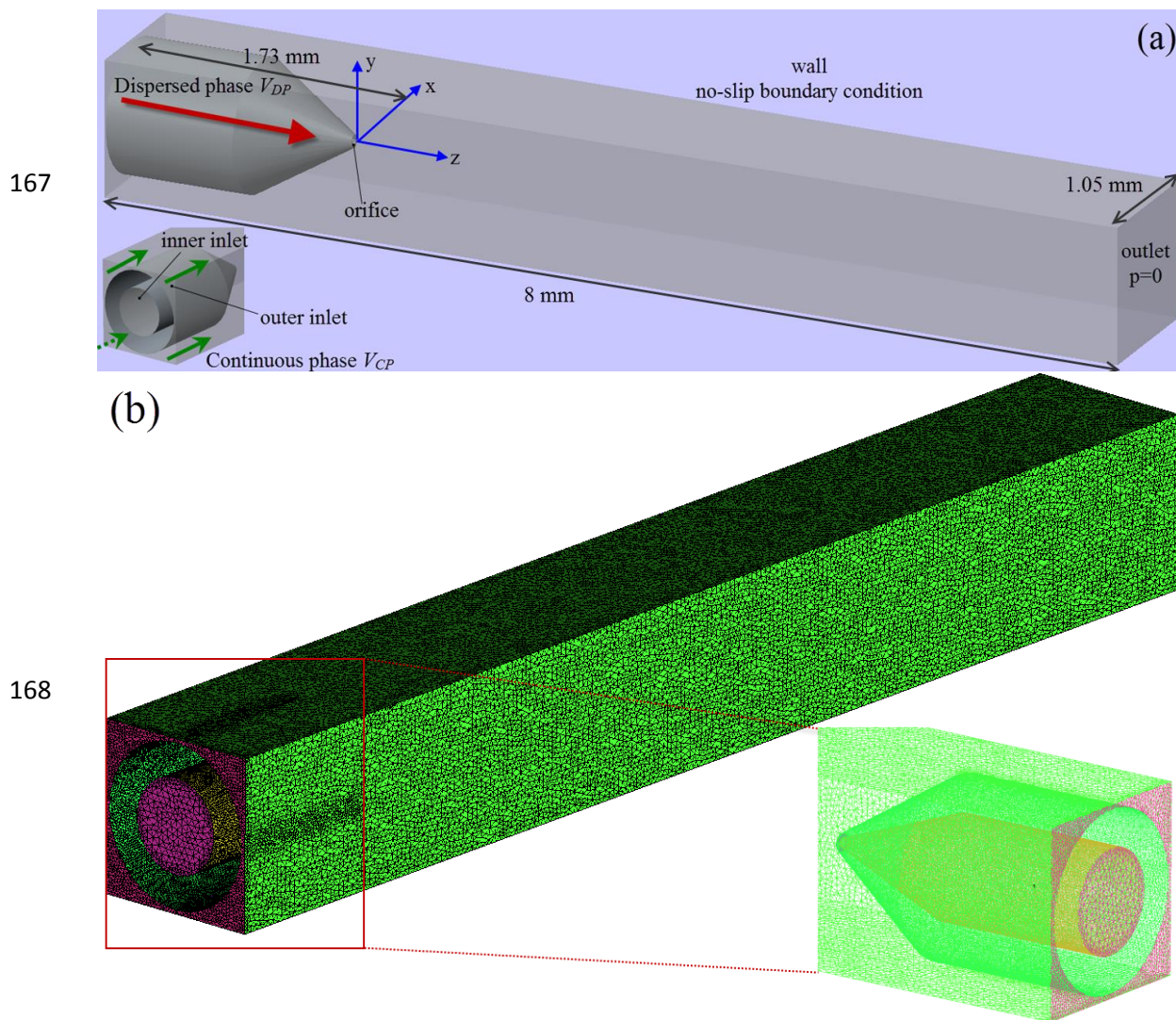
$$122 \quad \eta = \alpha_{CP} \eta_{CP} + (1 - \alpha_{CP}) \eta_{DP} \quad (7)$$

123 where V is the flow velocity, P is the pressure, ρ is the volume averaged density, α_{CP} and ρ_{CP} are
 124 the volume fraction and density of the continuous phase respectively, η_{DP} and η_{CP} are dynamic
 125 viscosities of the dispersed and continuous phases, respectively. The 3D numerical volume of
 126 fluid (VOF) model has been implemented to investigate the droplet breakup in pair of non-
 127 Newtonian/Newtonian fluids in T-shaped microchannel.²⁴The rheological property of the non-
 128 Newtonian continuous phase is modeled using Cross model, which has been widely applied in
 129 the modeling of industrial shear-thinning fluids.²⁵A shear-thinning fluid is used in our present
 130 study and its apparent viscosity is defined by,

$$131 \quad \eta_{CP} = \eta_{\infty} + \frac{\eta_0 - \eta_{\infty}}{1 + (\lambda_c \dot{\gamma})^n} \quad (8)$$

132 where η_{∞} refers to lower limiting values of the fluid viscosity or infinite shear viscosity; η_0 refers
133 to upper limiting values of the fluid viscosity or zero shear viscosity; λ_c is the time constant, the
134 reciprocal of which corresponds to a critical shear rate that provides a useful indicator of the
135 onset shear rate for shear thinning; $\dot{\gamma}$ is the shear rate in 3D flows, and is defined as the
136 magnitude of the rate of deformation tensor: $\dot{\gamma} = \sqrt{2(\mathbf{D}:\mathbf{D})}$, where \mathbf{D} is the rate of deformation;
137 and n represents the power law index of fluid. The solutions with different values of these
138 parameters will have different rheological behaviors. Any effect due to gravity is neglected for
139 simplicity, because the length scale of interest is much smaller than the capillary length of 1.33
140 mm in our model. The two-phase flow is solved using the VOF method by CFD software Ansys
141 Fluent 14.0. The approach has been successfully demonstrated to investigate multiphase flow in
142 microsystem.²⁶ The governing equations are discretized to algebraic equations by using a control-
143 volume-based technique. An iterative solver was deployed to solve the control-volume
144 discretized equations. The iterative time step is 10^{-7} s and the solution converges when the
145 residual is below a tolerance set as 1.0×10^{-6} . The simulations were performed using numerical
146 grids composed of triangular elements, as shown in Fig. 1b. The numerical data was subsequently
147 analyzed by Ansys CFX-Post 14.0 after simulation was completed. Computational sensitivity
148 study has been carried out to evaluate the effect of different triangular grid sizes. The generated
149 morphology of interface as indicated by the green color between dispersed and continuous
150 phases is compared using different grid sizes. Similar morphology is found at flow rates of the
151 dispersed phase $Q_{DP}=50$ ml/h, and of the continuous phase $Q_{CP}=70$ ml/h, as shown in Fig. 2. The
152 size of interface gradually increases along the axial direction, and subsequently adopts
153 cylindrical shape downstream with a uniform size for grid sizes of $4 \mu\text{m}$ and $8 \mu\text{m}$. The variation
154 in the generated size of interface is less than 5% after convergence between grid sizes of $4 \mu\text{m}$

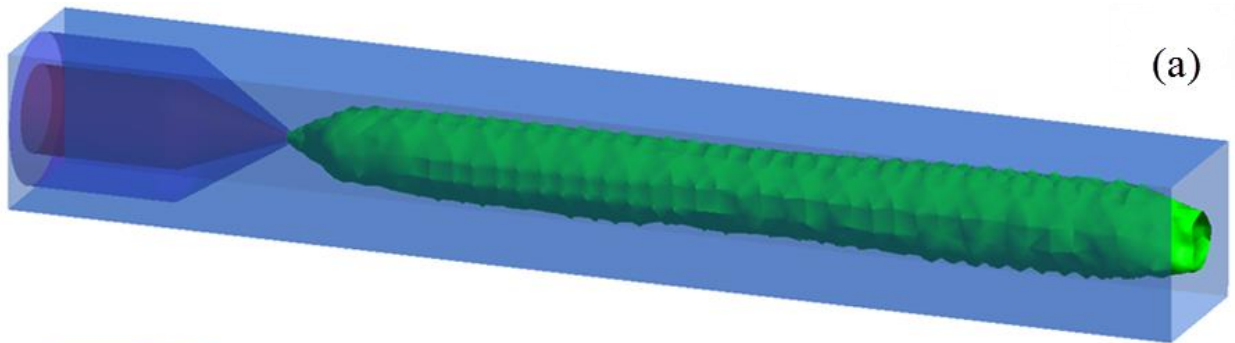
155 and $8\mu\text{m}$. Furthermore, we investigated the grid size effect by comparing numerical results of
156 axial velocity profile along transversal direction (x direction) for different grid sizes, at two
157 downstream locations, $z=0.02$ mm, where the two phases meet in vicinity of orifice, and $z=5.27$
158 mm, where the flow has become fully developed, as shown in Fig.3a-b, respectively. At $z=0.02$
159 mm, the sharp peak in the middle represents the velocity profile of dispersed phase, which is
160 purged out of orifice with very small size, thus the velocity will be increased dramatically due to
161 mass conservation. The magnitude of velocity for the continuous phase is much smaller, because
162 of the much larger cross section. At $z=5.27$ mm, the velocity profiles of dispersed and continuous
163 phases adjoin with a smooth transition at the interface. Compared with coarse grids with a size of
164 $12\mu\text{m}$, a good agreement is found between refined grids with a size of $4\mu\text{m}$ and $8\mu\text{m}$
165 respectively. 4300956 triangular elements with a size of $8\mu\text{m}$ are used in all the following
166 numerical simulations to reduce computation cost.



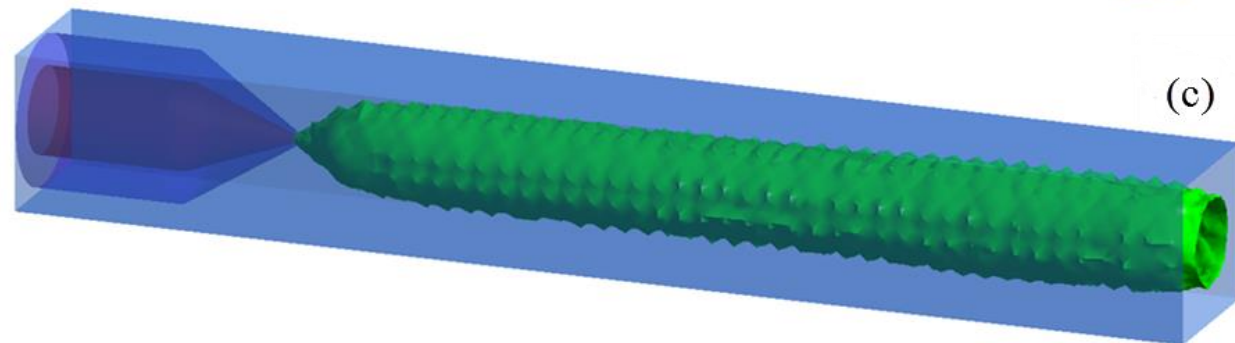
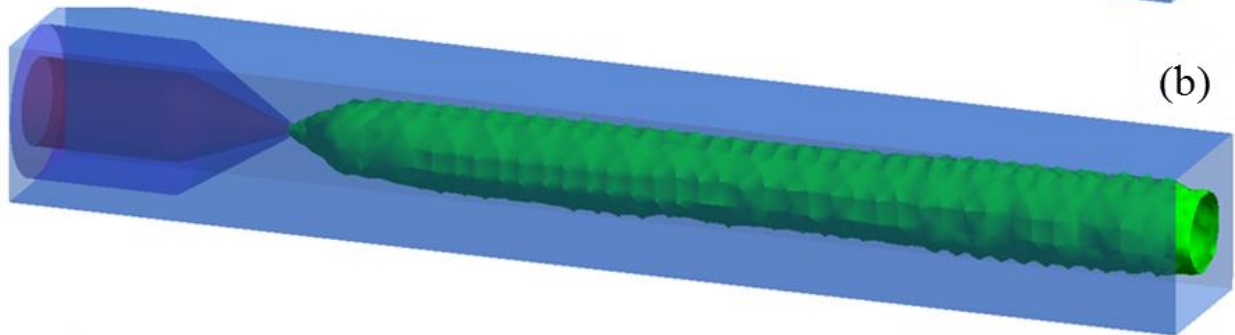
169 **Fig.1**(a) Schematic of the computational domain of multiphase microfluidic system. (b) Meshing
 170 grids. The close-up view of meshing of nozzle and inlets is shown in inset.

171

172



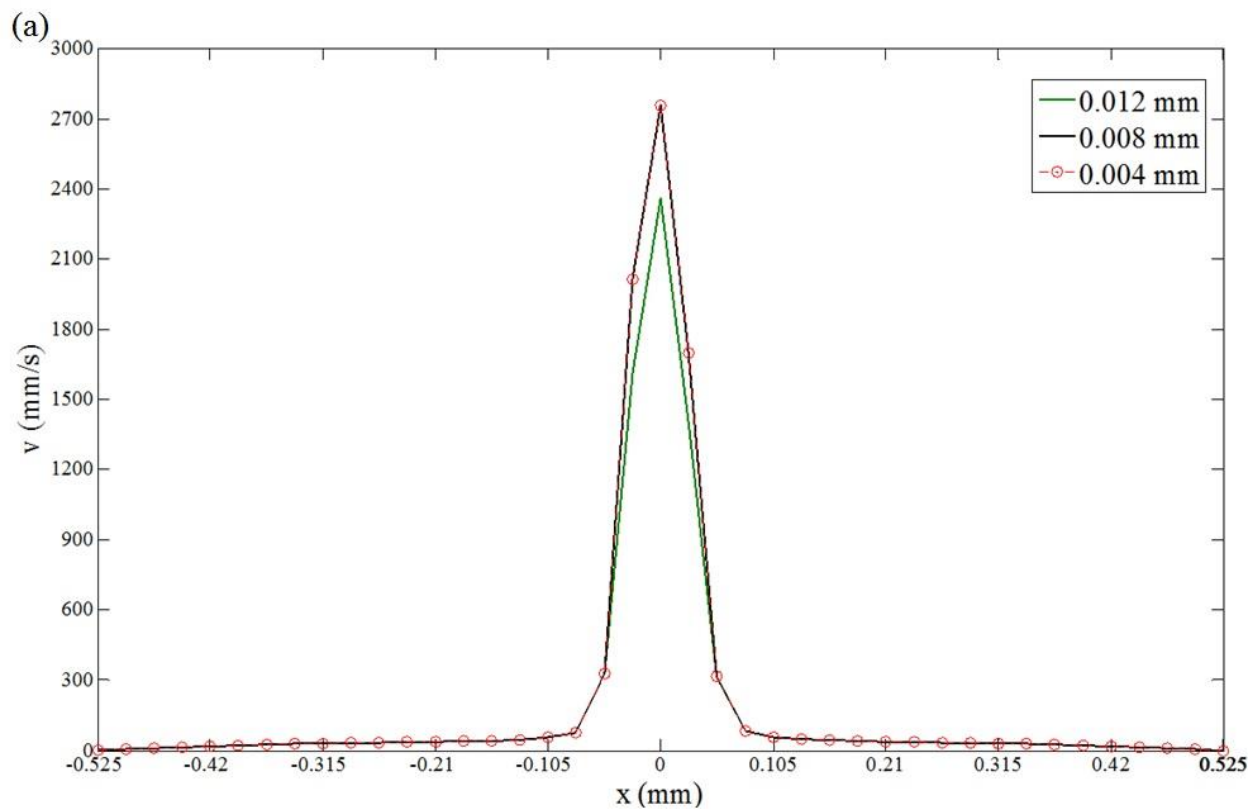
173



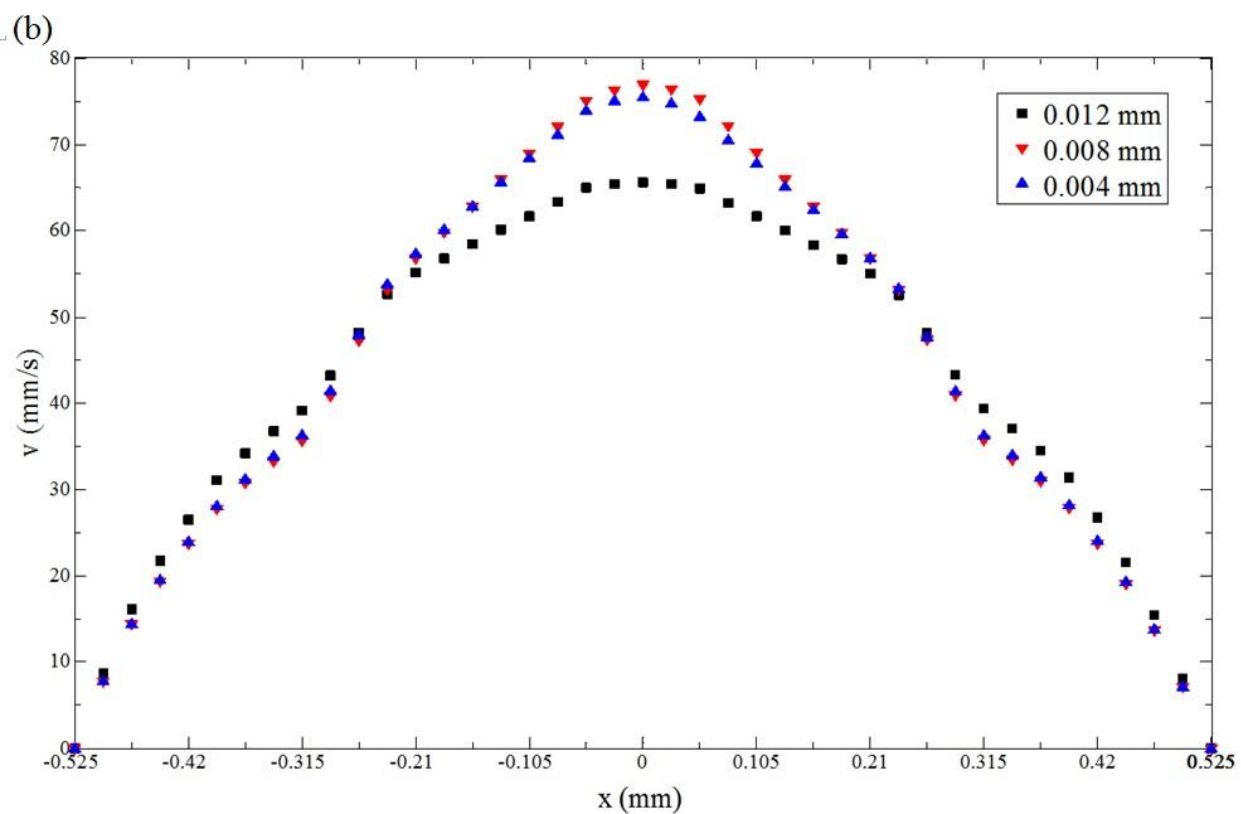
174 **Fig.2** Comparison of morphology of jet using different meshing grid sizes (a) 0.012 mm (b)

175 0.008 mm and (c) 0.004mm. $Q_{DP}=50$ ml/h, $Q_{CP}=70$ ml/h.

176



177



178 **Fig.3** Validation of the numerical model of Newtonian/shear-thinning multiphase microfluidic
179 system by comparison of axial velocity profile along transversal direction (x direction) at (a)
180 $z=0.02$ mm and (b) $z=5.27$ mm using different meshing grid sizes.

181 **3. Experimental section**

182 The Newtonian/shear-thinning two-phase co-flow is generated using a glass microcapillary
183 device reported earlier.²³ A glass slide was used as a substrate to support the capillary device,
184 which is composed of an inner round capillary (World Precision Instruments, Inc) and an outer
185 square capillary (Atlantic International Technology, Inc.). The round capillary has inner and outer
186 diameters of $630\ \mu\text{m}$ and $1.0\ \text{mm}$, and its tip was tapered to the desired diameter by a
187 micropipette puller (Sutter Instrument, Inc.) to obtain an orifice with an inner diameter of about
188 $49\ \mu\text{m}$. The tapered round capillary was fitted into the square capillary, which has an inner
189 dimension of $1.05\ \text{mm}$. Since the outer diameter of the round capillary matches with the inner
190 dimension of the square capillary, coaxial alignment of the two capillaries is ensured. The
191 dispersed phase was injected into the device through the circular capillary, while the continuous
192 phase was injected in the same direction through the square capillary. The fluids were injected
193 into the device through a flexible plastic tubing (Scientific Commodities Inc.), which was
194 connected to syringe pumps (Longerpump, LSP01-2A) at controlled flow rates. Unless otherwise
195 specified, the chemicals used in the study were supplied by Aladdin Reagents (Shanghai) Co.,
196 Ltd. In the present study, the dispersed phase was silicon oil, while the continuous phase was 2%
197 (w/v) aqueous solution of sodium carboxymethyl cellulose (CMC) ($M_w=250,000\ \text{Da}$, $DS=1.2$),
198 which is a pseudo-plastic fluid and demonstrates shear-thinning behaviors. The rheological
199 behavior of CMC solution can be characterized by two critical concentrations: ²⁷ a first critical

200 CMC concentration indicates the transition to the semidilute network solution, while a second
201 critical CMC concentration indicates the transition to the concentrated solution. Below the
202 second critical concentration, the CMC solution becomes highly viscous and the dynamics is
203 dominated by viscous effects; above the second critical concentration, the dynamics become
204 dominated by elastic effects. For CMC solution with a nominal molecular weight of 700,000 Da
205 and a degree of substitution of 0.65-0.85, the first critical concentration is ~1% while its second
206 critical concentration is 2.5%.²⁷The effect of concentration and molecular weight on the
207 rheological behavior of aqueous CMC solutions has been investigated experimentally.²⁸Based on
208 their measurements of the rheological properties, solutions of CMC with molecular weights of
209 90,000 Da, 250,000 Da, and 700,000 Da all exhibit predominantly shear-thinning behaviors over
210 a shear rate of 0-1000 /s in absence of yield stress as their concentration changes from 0.1% to
211 3.0%. The average shear rate of CMC solution is below 1000 /s by controlling flow rate in our
212 work. Therefore, it is reasonable to assume that our CMC solution (Mw=250,000 Da, DS=1.2)
213 still has a predominantly viscous behavior; and the elastic effect can be ignored.²⁸

214 We also prepared 5% (w/v) aqueous solution of polyacrylamide (PAA, supplied by Wing Hing
215 Chemical Co., Ltd) as the continuous phase to investigate the elastic effect on the breakup
216 dynamics and droplet formation. The flow behavior inside the microcapillary device was
217 monitored with an inverted microscope (Motic, ocular: WF10×18mm, object lens: EA4). A high-
218 speed camera (Phantomv9.1 high speed camera) was connected to the microscope and the flow
219 through the capillary was captured. The dripping-to-jetting transition using non-Newtonian
220 systems was characterized experimentally, and the breakup dynamics in a non-Newtonian fluid
221 system was compared with a Newtonian fluid system at the same Weber number and Capillary
222 number using the same microdevice. For the Newtonian two-phase flow, silicone oil was also

223 used as the dispersed phase, while 17% w/v aqueous solution of polyethylene glycol (PEG)
224 (Mw=8,000 Da) was used as the continuous phase. The interfacial tension was measured by a
225 Kruss spinning drop tensiometer-SITE100. The respective viscosity of each solution was
226 measured at different shear rates by a Brookfield DV-II+Pro programmable viscometer. Shear-
227 thinning behavior of the CMC solution was observed experimentally. The rheology data of CMC
228 solution at all concentrations can be well represented by the well-known Cross model;²⁷ therefore
229 Cross model was used in curve-fitting of the experimental data, and the measured Cross model
230 parameters (the zero shear viscosity $\eta_0=253.5$ cP, infinite shear viscosity $\eta_\infty=60$ cP, and the
231 flow index $n=0.9$, as shown in Fig.4) were used in the simulation for computing the simulation
232 results, which were subsequently compared with the experimental observations. As a comparison,
233 we also use the Carreau model in curve-fitting of the experimental data of the CMC solution.
234 The agreement with the experiment value is not as good as that with the Cross model. The fitting
235 quality of the two models was evaluated by the corresponding standard deviation and Pearson
236 correlation coefficient,²⁹ which are 0.329 and 0.934 respectively for the Carreau model, and
237 0.095 and 0.980 respectively for the Cross model. The smaller standard deviation and larger
238 Pearson correlation coefficient suggest that the rheological behavior of CMC solution is better
239 modelled using the Cross model; thus Cross model is picked over the Carreau model. Very small
240 variations of viscosity were observed at different shear rates (see Fig.4), indicating that 17% w/v
241 PEG solution exhibits largely Newtonian properties. The concentration of PEG solution can
242 affect the rheological property. For example, 7% w/w PEG solution shows significantly different
243 viscosity values at different shear rates, demonstrating a non-Newtonian behavior.³⁰ 5% w/v PAA
244 solution possesses shear-thinning behavior, as shown in Fig.4. As a typical viscoelastic liquid,
245 the rheology property of PAA has been well investigated, and the storage modulus G' and loss

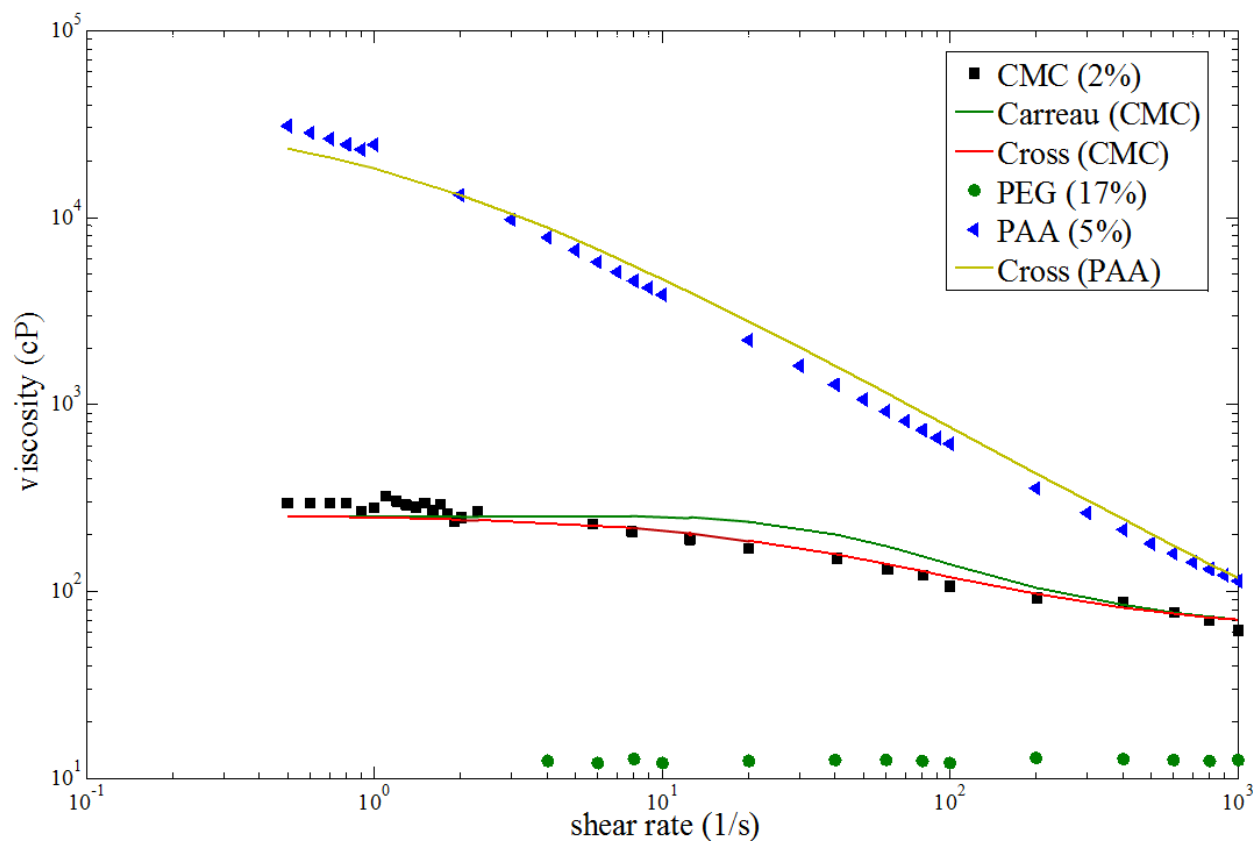
246 modulus G'' have been measured using the oscillatory shear rheometer.³¹ Based on the reported
 247 data, we find the relaxation time $\lambda=0.017$ s, according to Maxwell model of viscoelastic
 248 liquid.³² The relevant dimensionless numbers of viscoelastic liquid include Weissenberg number
 249 Wi and Elasticity number El . The Weissenberg number is defined as the product of the relaxation
 250 time and a characteristic rate of deformation of the flow, and quantifies the nonlinear response of
 251 the liquid.

$$252 \quad Wi = \frac{\lambda U}{D_t} = \frac{\lambda Q_{CP}}{D_t^3} \quad (9)$$

253 where U is the average axial flow velocity in the capillary device and D_t refers to the dimension
 254 of the capillary tube. Wi is dependent on flow rate and varies in the range between 0.0041 and
 255 0.041 in our experiments. The ratio between elastic and inertial effects is represented by the
 256 Elasticity number,

$$257 \quad El = \frac{Wi}{Re} = \frac{\lambda \eta_{CP,0}}{\rho_{CP} D_t^2} \quad (10)$$

258 where Re refers to Reynolds number. El is thus independent on the flow rate based on the
 259 definition. In our experiments $El=382$, indicating the dominating role of elastic effect relative to
 260 inertia effect. The physical properties of the fluids used in the investigation are shown in Table 1.



261

262 **Fig.4** Rheological properties of the three aqueous polymer solutions: 2% w/v sodium
 263 carboxymethyl cellulose (CMC) in water (black squares), 17% w/v polyethylene glycol (PEG) in
 264 water (green circles), 5% w/v polyacrylamide (PAA) in water (blue triangle), Cross model of
 265 CMC solution (red solid line), Carreau model of CMC solution (green solid line) and Cross
 266 model of PAA solution (yellow solid line).

267
268

269

270

271

272

273 **Table 1**

274 Physical property of the test fluids

Test fluids	η (cP)	ρ (g/ml)	σ (mN/m) (silicon oil and CMC)	σ (mN/m) (silicon oil and PEG)	σ (mN/m) (silicon oil and PAA)
Silicon oil	10	0.963			
CMC (2%)	253.5 (zero- shear rate)	0.990			
PEG (17%)	13.6	1.053	7.12	9.624	10.176
PAA (5%)	24569(zero- shear rate)	0.992			

275

276 **4. Results and discussion**

277 The breakup dynamics and dripping-to-jetting transition in Newtonian/shear-thinning multiphase
278 microsystem are presented and discussed first, followed by discussion of elastic effect in droplet
279 shape at the end of this section. Simulation and experiments of Newtonian/shear-thinning
280 multiphase flow in the capillary microdevice have been conducted under the same flow
281 conditions to observe the process of jet deformation and droplet formation. Silicon oil and CMC
282 solution are used as dispersed phase and continuous phase, respectively. The flow pattern at
283 successive time points from simulation is shown in Fig.5. The flow rates of the dispersed and
284 continuous phases are 5 and 7 ml/h, respectively, with $Ca_{out} = 0.0631$ and $We_{in} = 5.147$. The
285 transition regime is observed and the jet size changes along the length of jet. The dispersed phase
286 is purged out of the orifice, as shown by the inset in Fig.5a. The droplet grows in size and moves
287 downstream while it is still connected to the fluid neck through the orifice via a filament, as
288 shown in Fig.5b. The filament gradually becomes thinner (see Fig.5c) and finally breaks up into

289 a droplet (see Fig.5d). The process is repeated afterwards. The interface between the two phases
290 in Fig.5d is tracked by plotting the radius of interface along transversal direction (y direction)
291 versus the streamwise location along z direction. The simulation result is represented by the solid
292 line, and is compared with experimental measurements indicated by the symbols. A reasonable
293 agreement, as shown in Fig.5e, validates the accuracy of the numerical model.

294 A satellite droplet is formed during the breakup of an elongated filament between two adjacent
295 droplets. The profile near the breakup point is highly asymmetric, with the droplet interface
296 being very steep towards the droplet while lying flat towards the neck of the jet. The existence of
297 satellite drops is intimately related to the non-linear properties of the fluid motion close to the
298 breakup point.³³ When the filament breaks at both ends before merging with one of the parent
299 droplets, the filament separates from both neighboring parent droplets and recoils into a satellite
300 droplet.³⁴ The number of satellite droplets and their relative sizes strongly depend on the viscosity
301 ratio of the dispersed phase to that of the continuous phase, and are also influenced by the initial
302 disturbance wavenumber, which is defined as $2\pi a/\varepsilon$, where a is the radius of filament and ε is the
303 wavelength.³⁵ At a small viscosity ratio, the slender center droplet undulates and pinches off at a
304 number of locations, generating a string of small satellite droplets. By contrast, when the
305 viscosity ratio is large, the internal flow leading to breakup is attenuated, resulting in the
306 formation of fewer satellite droplets. As the wave number increases, the ratio of radius of
307 satellite droplets in different birth regions relative to radius of parent droplet also increases.³⁵

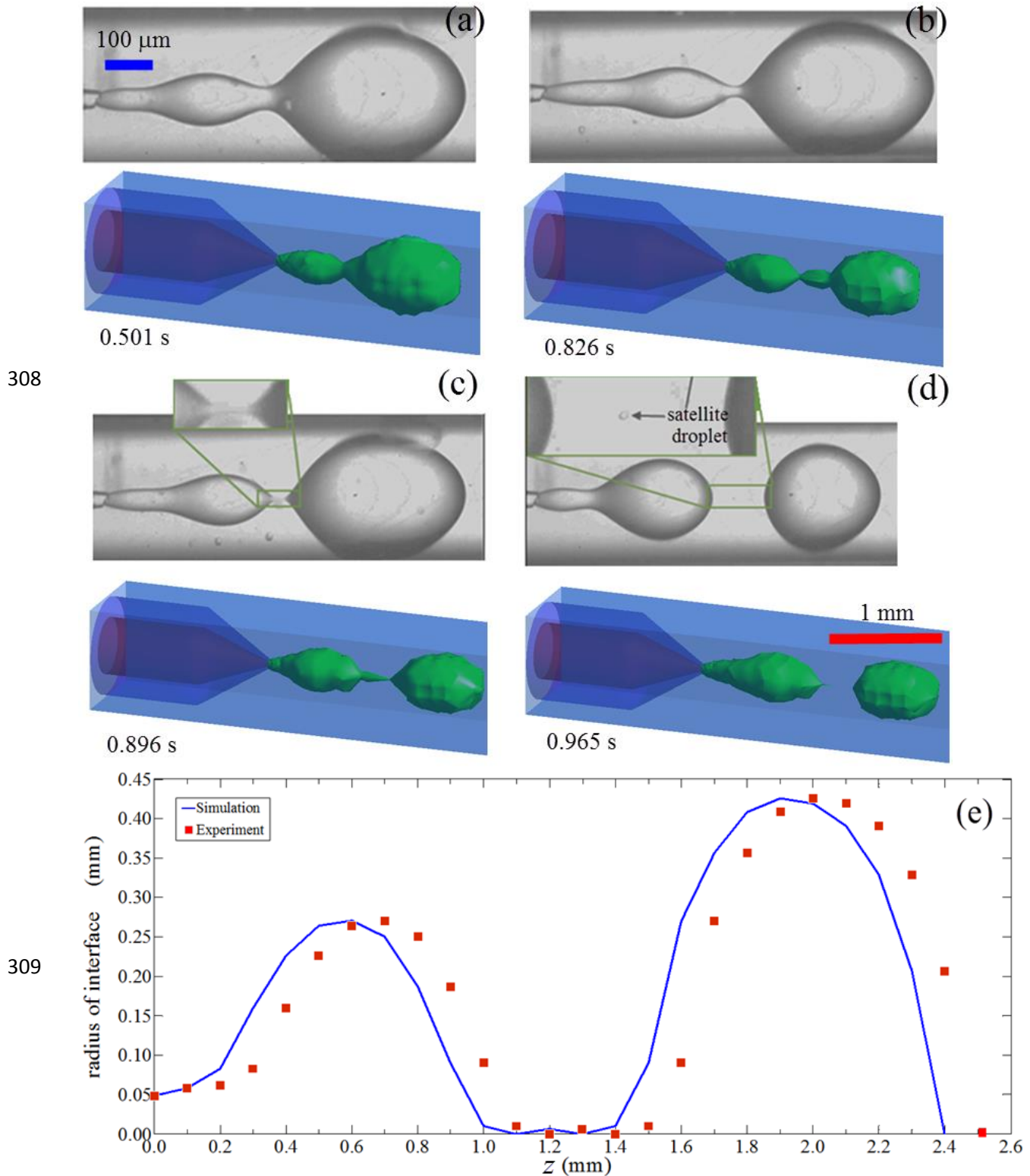
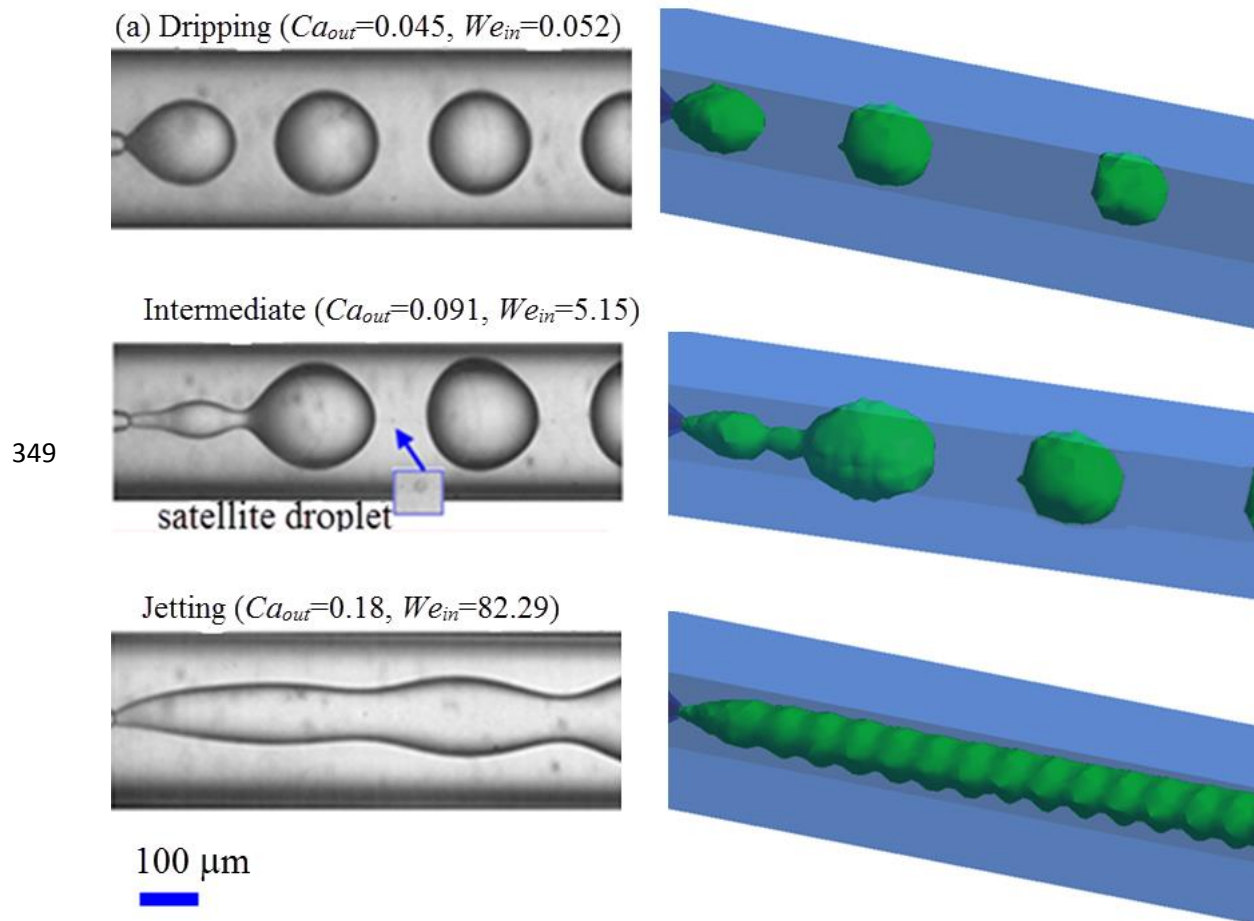


Fig.5 Time-lapse images of jet deformation and droplet formation from simulation (upper one in each sub-figure) and experiments (lower one in each sub-figure) using a Newtonian/shear-

312 thinning two-phase co-flow system (silicon oil as dispersed phase and CMC solution as
313 continuous phase). The blue and red scale bars are applicable for the experimental and
314 simulation results respectively. (a) The dispersed phase is purged out of the orifice; (b) The main
315 droplet is connected with the fluid neck via a thin filament; (c) The filament becomes even much
316 thinner; (d) Satellite droplet occurs after breakup of the jet; (e) Tracking of interface profile by
317 both simulation and experimental observation.

318 Since the satellite droplets have a much smaller size than the main droplet, the global
319 polydispersity of the resultant emulsion increases. To predict the occurrence of satellite droplets,
320 the flow conditions that result in the formation of satellite droplets have been delineated using a
321 state diagram, which shows the two-phase flow pattern as a function of Weber number and
322 Capillary number. Three representative flow regimes are observed when the flow rate ratio is
323 varied, as shown in Fig.6a: dripping, where droplets are formed in the vicinity of the capillary tip;
324 intermediate, where the growing droplets move downstream while remaining connected to the
325 fluid in the tip through a fluid neck;¹⁸ and jetting, where droplets breaks up from an extended jet
326 with an incomplete retraction of the fluid neck. For the intermediate regime, the fluid neck
327 retracts completely back to the tip after the droplet pinches off at the detachment point of the
328 fluid neck. This regime is thus still regarded as dripping.¹⁸ Upon further increase of viscous or
329 inertia force, for instance, by changing the flow rate of continuous or dispersed phase, the
330 intermediate regime will transition to the jetting regime. Comparison of results from simulation
331 and experiments shows a good agreement, confirming the validity of our model in capturing the
332 physical behavior of the two-phase flow when a non-Newtonian fluid is used. As We_{in} increases,
333 the viscosity of the shear-thinning continuous phase decreases, when subjected to high shear rate.
334 As a result, a lower viscous stress is exerted on the dispersed phase; the liquid thread is therefore

335 not pulled further downstream. Consequently, the flow remains in the intermediate regime rather
336 than in the jetting regime. However, when We_{in} is larger than 10, jetting occurs because of the
337 larger inertial force. Based on experimental observation, satellite droplets appear only in the
338 intermediate regime, which is characterized as a dripping-to-jetting transition,¹⁸ as shown in the
339 state diagram in Fig.6b. Inertia is necessary to induce the formation of a satellite droplet, because
340 the droplet formation will be suppressed when the viscous force is dominant over inertia.
341 However, a very large inertial force will lead to formation of jetting and the liquid thread will
342 breakup into droplets further downstream. Consequently, the pinch-off time increases, delaying
343 the formation of the parent droplet and satellite droplets. This state diagram can help predict the
344 formation of undesirable satellite droplets in a Newtonian/shear-thinning two-phase system, and
345 can suggest operating conditions for eliminating satellite droplets. This ultimately inspires
346 production of monodisperse droplets by manipulating the breakup profile and controlling the
347 merging of satellite droplets with main droplets; yet these investigations are beyond the scope of
348 the present study.



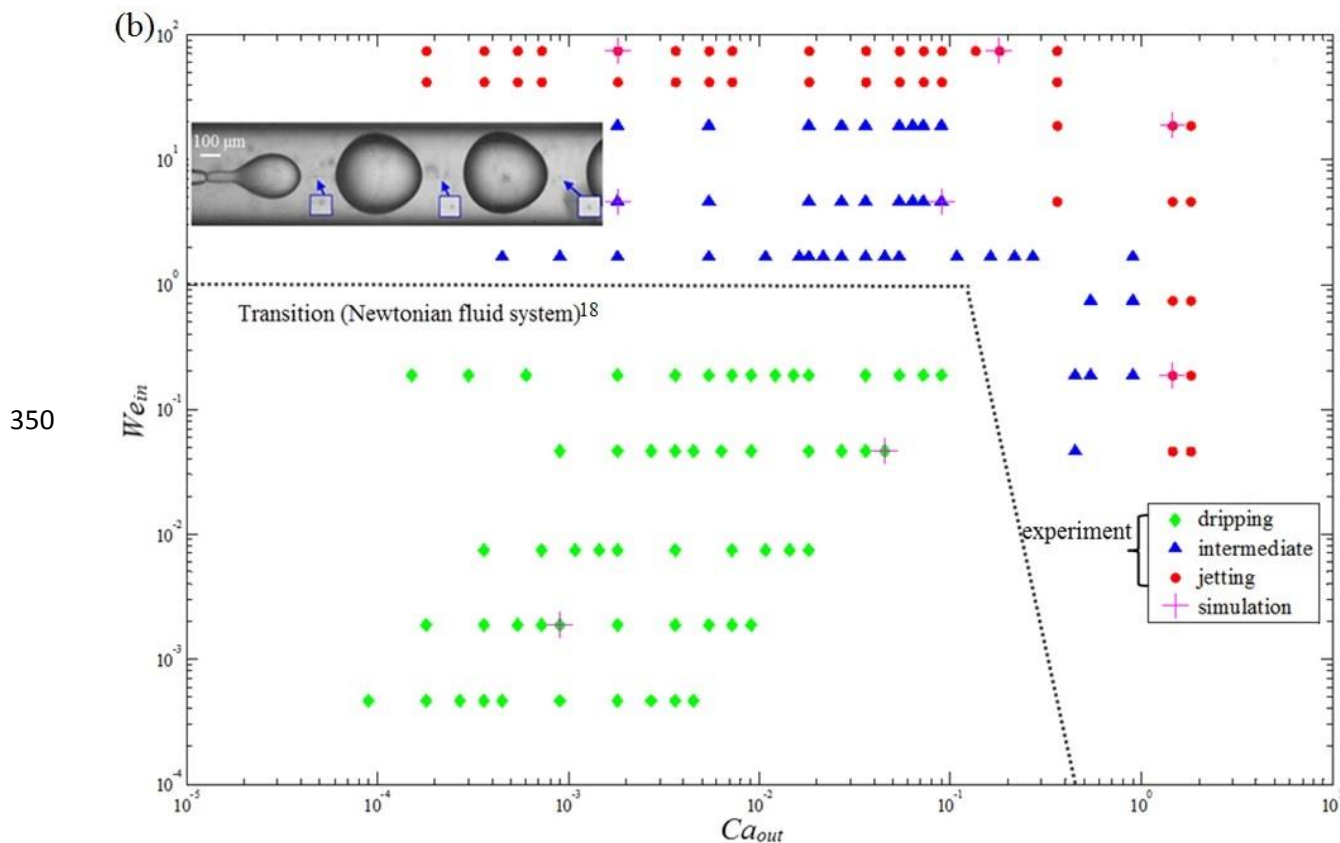


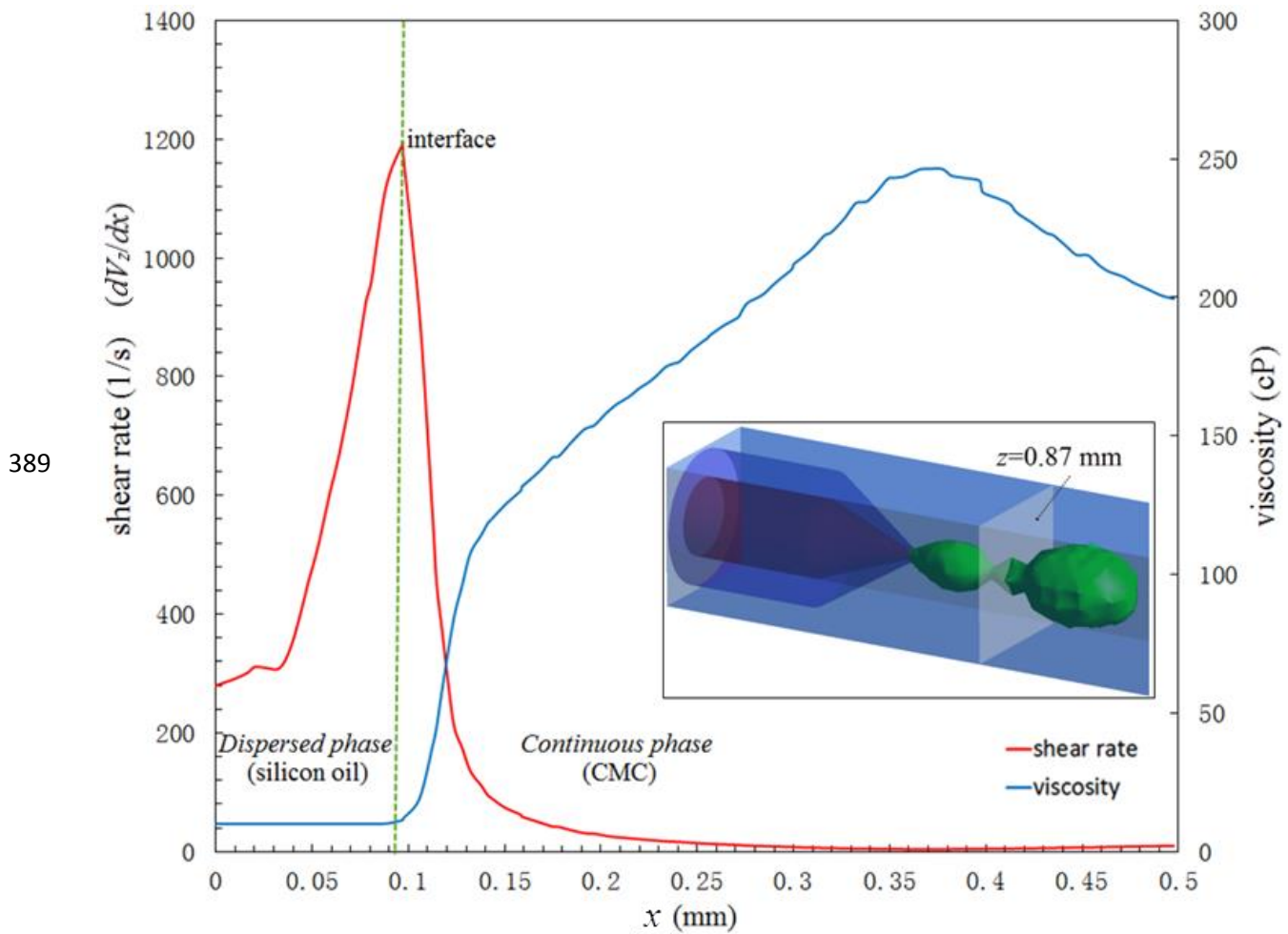
Fig.6(a) Comparison of results from simulation and experiments at different regimes using a Newtonian/shear-thinning two-phase coflow system (silicon oil as dispersed phase and CMC solution as continuous phase). (b) State diagram showing the dripping-jetting transition as a function of Ca_{out} and We_{in} . The inset shows the satellite droplets appearing periodically between adjacent parent droplets. The dash line (Reprinted (figure 4) with permission from [ref.18] as follows: Utada et al., Phys. Rev. Lett. 99, 094502, 2007. Copyright (2014) by the American Physical Society) shows the dripping-to-jetting transition in a purely Newtonian two-phase coflow system (deionized water and polydimethylsiloxane (PDMS) oils). The breakup time is one of the determining factors on the droplet production rate. It is thus of fundamental interest and industrial relevance to investigate the breakup time when non-Newtonian fluids, for example, shear-thinning fluids, are used, in comparison to the counterpart

362 of Newtonian multiphase system at the same We_{in} and Ca_{out} . Droplet breakup occurs due to the
 363 interplay between the viscous stress and the interfacial tension between the two fluids. The
 364 viscous stress is closely associated with the shear rate, which varies greatly depending on the
 365 position. The shear rate affects the viscosity in all directions in the 3D flow. The highly
 366 deformed filament connecting the fluid neck with the droplet (see Fig.5b) is of particular interest,
 367 because it is the region where breakup occurs. We will therefore use the filament region, for
 368 instance, $z=0.87$ mm, as the focal point to characterize the shear-rate-dependent viscosity profile.
 369 Given the continuity of velocity at the interface and the small diameter of filament, the shear rate
 370 reaches a sharp peak at the interface between the two phases in the filament region. Due to shear-
 371 thinning characteristics of CMC solution, the viscosity will be dramatically reduced at the
 372 interface, as shown by the numerically calculated results of viscosity and shear rate as a function
 373 of the radial location along the transverse direction of the capillary device in Fig.7. The
 374 magnitude of shear rate of the continuous phase in the co-flowing microfluidic device with a
 375 dimension of D_t is related to the droplet diameter D_d through,²⁶

$$\dot{\gamma} \sim \frac{Q_{CP}}{\pi D_t^3 [1 - (\frac{D_d}{D_t})^2] (1 - \frac{D_d}{D_t})} \quad (11)$$

377 The expression suggests that a droplet with fixed size will be subject to larger shear rate when
 378 the flow rate increases, and that a droplet with larger size will induce a higher shear rate at a
 379 fixed flow rate, because the larger droplet will tend to disrupt and confine the flow of continuous
 380 phase, unless the dimension of microcapillary tube can be changed. Given the flow condition in
 381 Fig.5, where $Q_{CP}=7$ mL/h and $\frac{D_d}{D_t} = 0.5$, $\dot{\gamma} \sim 1.65/s$. The calculated shear rate of the continuous
 382 phase is of the same order of magnitude as the simulation result of shear rate, which refers to the

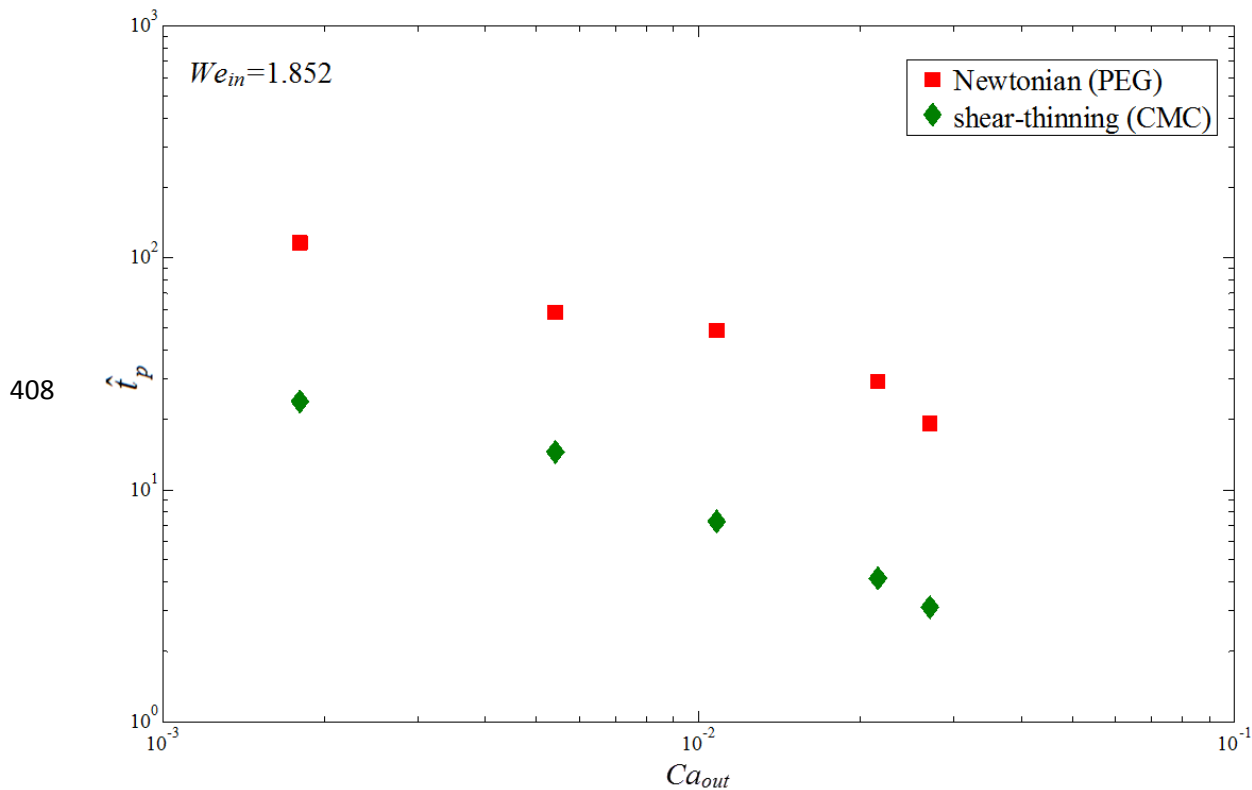
383 derivative of the axial flow velocity with respect to the radial coordinate, dV_z/dx , in Fig.7. A
 384 local maximum shear rate of 9.68/s for continuous phase is obtained at the wall of collection tube,
 385 because of no-slip at the wall and large velocity gradient in boundary layer adjacent to the wall.
 386 The shear rate is reduced in the region far from the wall, and the minimum value of 3.87/s is
 387 obtained at $r=0.375$ mm.
 388



390 **Fig. 7** The numerically calculated viscosity and shear rate as a function of the radial position
 391 along the transverse direction of the capillary device of the Newtonian/shear-thinning two-phase

392 coflow system (silicon oil as dispersed phase and CMC solution as continuous phase) at $z=0.87$
393 mm, which is illustrated in inset.

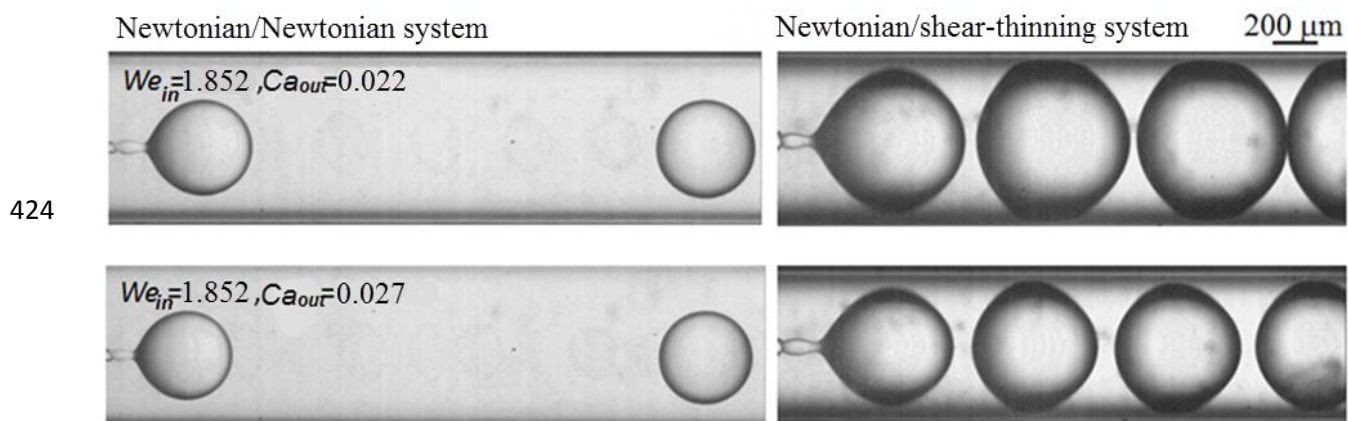
394 For shear thinning fluids, the viscosity is inversely proportional to the shear rate; thus the viscous
395 effect will be attenuated near regions with high shear rate, facilitating the pinch off of the jet.
396 Consequently, the breakup process will be sped up so that a higher production rate of droplets
397 can be expected. To verify the hypothesis that shorter breakup time can be achieved when a
398 shear thinning fluid is involved, control tests have been conducted to monitor the breakup time
399 for the purely Newtonian two-phase system. The dimensionless pinching time,
400 $\hat{t}_p = t_p / t_v = t_p / (\eta_0 d / \sigma)$, was measured experimentally at the same We_{in} and Ca_{out} , where t_p and
401 t_v refer to the measured time interval between two successive pinching, and the viscous time
402 scale, respectively. When compared with the Newtonian system with constant viscosity, the
403 shear-thinning fluid near the liquid-liquid interface has a much reduced viscosity due to high
404 shear rate; as a result, at the same Capillary number, surface force dominates and the pinching is
405 faster when a shear-thinning fluid is used as the continuous phase. The dimensionless breakup
406 time is also reduced when Ca_{out} increases due to the enhanced viscous shear stress exerted on the
407 droplets, as shown in Fig. 8 where $We_{in}=1.852$.



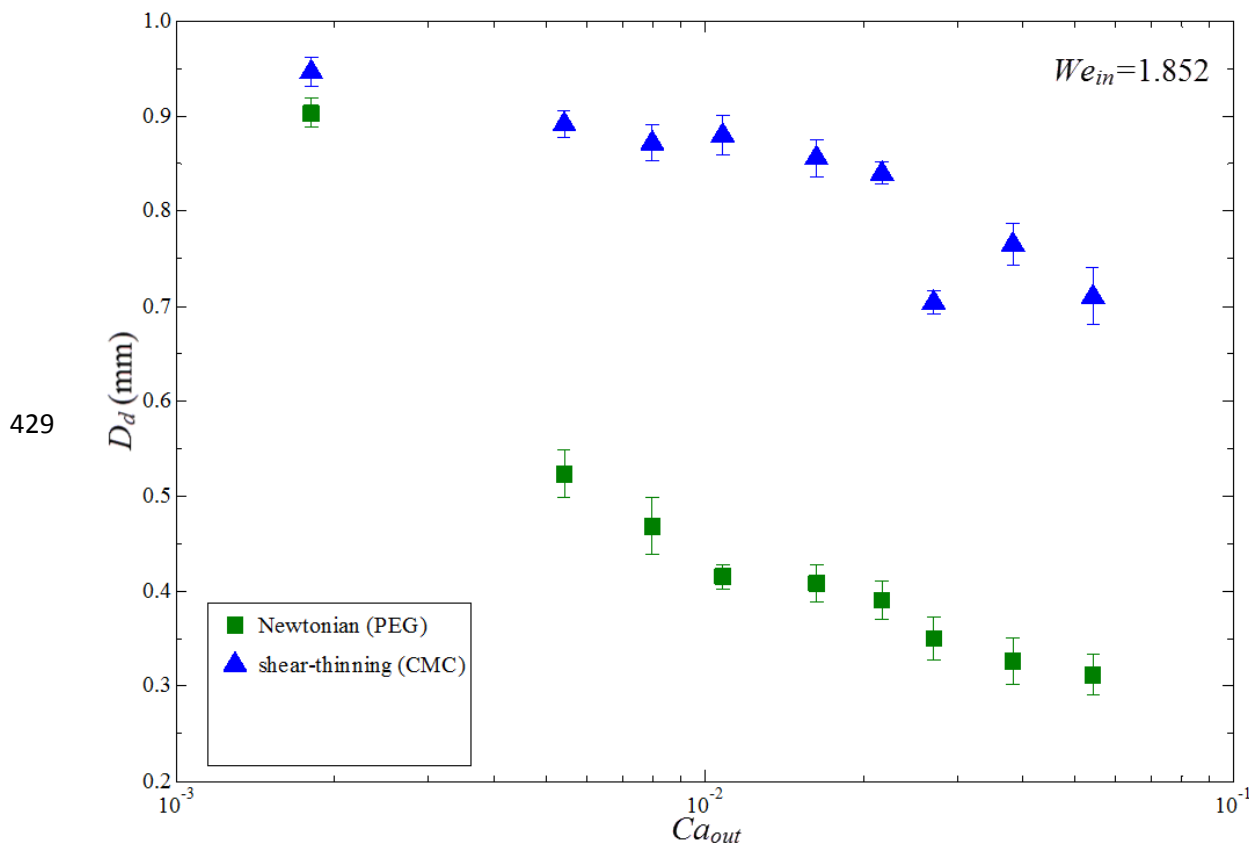
409 **Fig.8** Comparison of the experimentally observed breakup time of jet into droplets using the
 410 Newtonian/shear-thinning two-phase coflow system (silicon oil as dispersed phase and CMC
 411 solution as continuous phase) versus Newtonian/Newtonian two-phase coflow system (silicon oil
 412 as dispersed phase and PEG solution as continuous phase) when $We_{in}=1.852$.

413 In the breakup process of liquid jet of dispersed phase, the droplets are formed and surrounded
 414 by the continuous phase. The droplet size is influenced by the viscous force and the surface
 415 tension force. Due to the reduced viscosity of the continuous phase, the droplet size is larger
 416 when a shear-thinning fluid is used at the same We_{in} and Ca_{out} .³⁶This is confirmed by the
 417 observed snapshots of droplets after breakup at the same Weber number but at different Capillary
 418 numbers in two different multiphase systems, as shown in Fig.9. In both cases, silicone oil is
 419 used as the dispersed phase, while solutions of PEG and CMC are used as the Newtonian and

420 non-Newtonian continuous phases respectively. At the same Weber number of 1.852, both
 421 systems show a decrease in the droplet size when the Capillary number is increased from 0.0018
 422 to 0.054 (see Fig.10), due to the higher shear stress and the enhanced hydrodynamic focusing
 423 effect by the continuous phase.



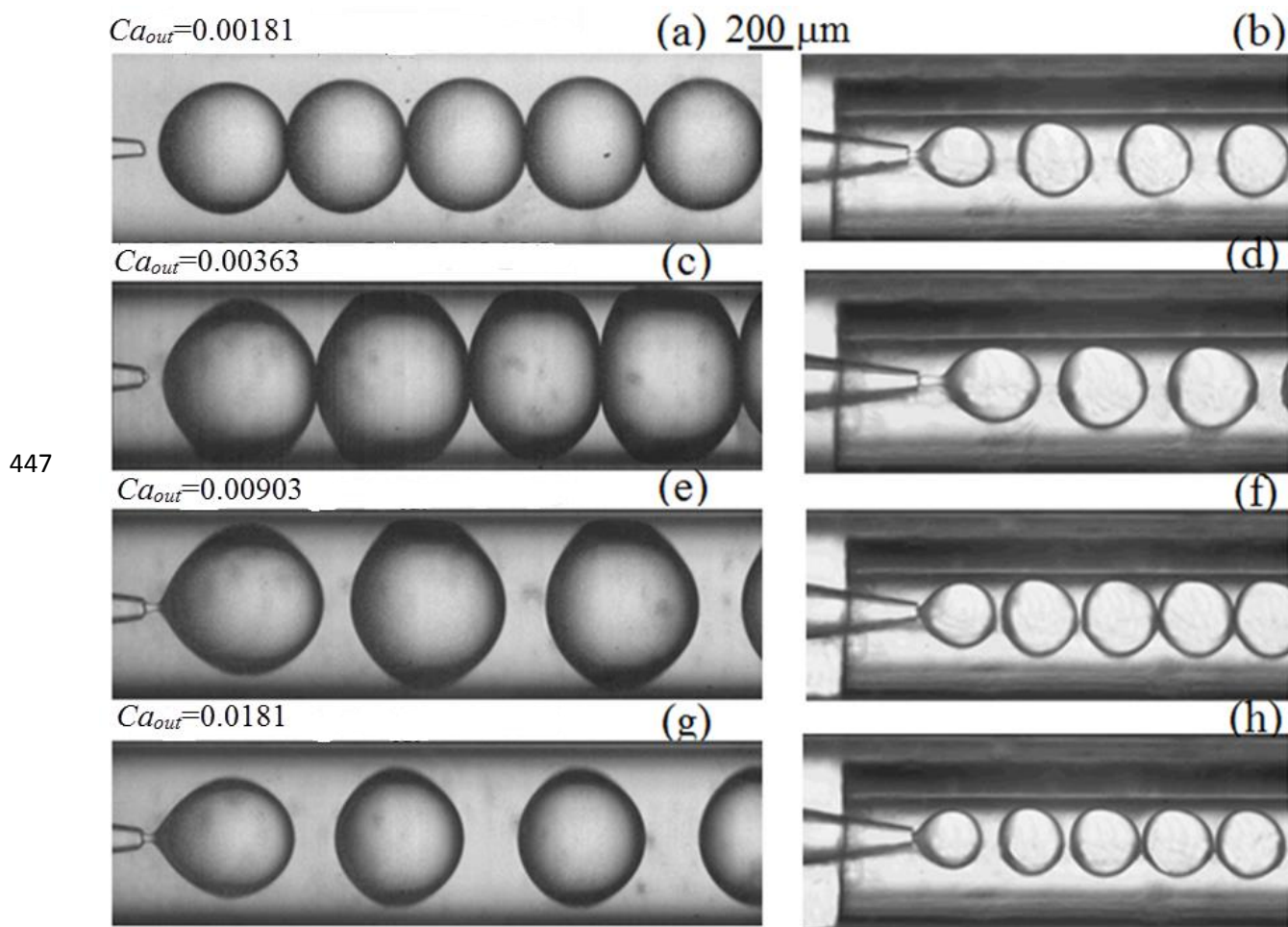
425 **Fig.9** Comparison of droplet size between Newtonian/shear-thinning two-phase coflow system
 426 (silicon oil as dispersed phase and CMC solution as continuous phase) and
 427 Newtonian/Newtonian multiphase coflow system (silicon oil as dispersed phase and PEG
 428 solution as continuous phase).



429
430 **Fig.10** Comparison of the experimentally observed droplet diameter between the
431 Newtonian/shear-thinning two-phase system (silicon oil as dispersed phase and CMC solution as
432 continuous phase) and the Newtonian/Newtonian two-phase system (silicon oil as dispersed
433 phase and PEG solution as continuous phase). $We_{in}=1.852$ in all cases.

434 Control of the droplet size is also an important aspect of droplet-based microfluidic applications.
435 For example, the volume of the droplet which contains reagents or analytes is one of the key
436 parameters that determine the efficiency and the overall throughput of the system.³⁷ Since non-
437 Newtonian fluids are ubiquitous in biochemical applications of microfluidics, it is also crucial to
438 control droplet size. To achieve smaller droplets, we vary the dimensions of the nozzles by
439 fitting a round capillary with radius R into the square capillary (see Fig.11). At a constant flow
440 rate of outer-phase and constant Capillary number, evaluated based on the apparent viscosity, the

441 shear rate increases with decreasing inner diameter of the collection capillary, leading to an
 442 increase in the shear stress and thus reduced droplet sizes, as shown by the observed droplets in
 443 the collection tube with two different sizes in Fig.11. The droplet size is significantly reduced
 444 when collection tube with a smaller radius of 0.3mm is used (see the sub-figures on the right) as
 445 compared to that with a radius of 0.5 mm (see the sub-figures on the left), at the same Weber
 446 number and Capillary number.



448 **Fig.11** Observed droplets in collection tubes with different sizes ($R=0.5\text{mm}$ in a, c, e and g;
 449 $R=0.3\text{ mm}$ in b, d, f and h) using Newtonian/shear-thinning two-phase system (silicon oil as

450 dispersed phase and CMC solution as continuous phase). $Ca_{out}=0.00181$ in a-b, $Ca_{out}=0.00363$ in
 451 c-d, $Ca_{out}=0.00903$ in e-f, and $Ca_{out}=0.0181$ in g-h. $We_{in}=0.206$ in all cases.

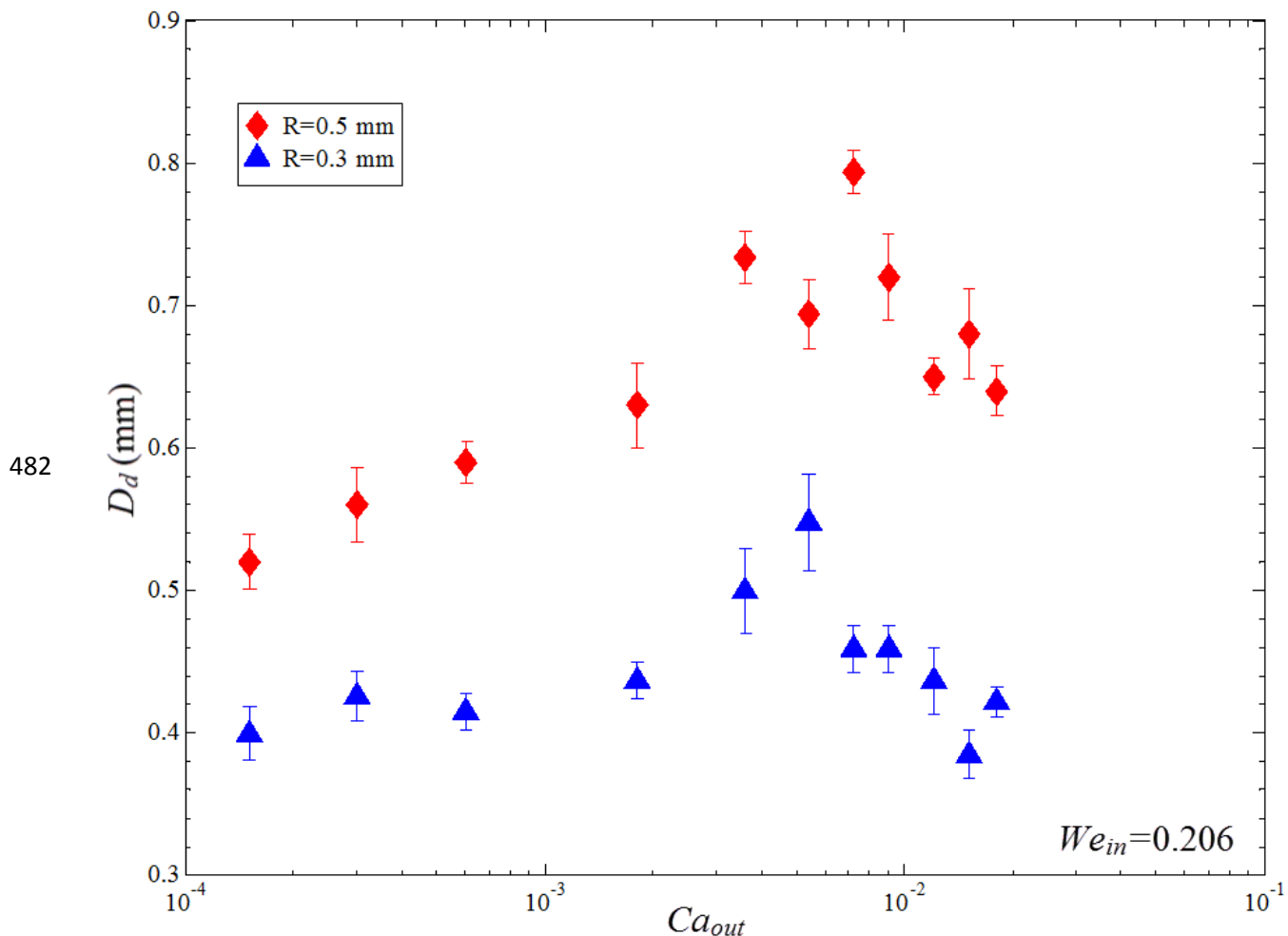
452 As Ca_{out} and the shear rate of continuous phase increase, the viscosity of continuous phase is
 453 reduced for shear-thinning fluids such as CMC; this results in larger droplets.³⁶ However, when
 454 Ca_{out} increases beyond a critical value, the viscous drag can overcome the surface tension effects
 455 that would otherwise minimize the stretching of the fluid neck by drawing the fluid interfaces
 456 closer to the orifice. As a result, the fluid neck becomes stretched and elongated at high Ca_{out} .

457 When a round capillary with a radius R is inserted into the square capillary, we consider the
 458 shear rate of continuous phase that flows by the fluid neck of dispersed phase with a radius r_j ; D_t
 459 can be replaced by $2R$, and D_d can be replaced by $2r_j$ in Eq. (11). Therefore, the shear rate is
 460 defined by,

$$461 \quad \dot{\gamma} \sim \frac{Q_{CP}}{\pi(D_t^2 - D_d^2)(D_t - D_d)} = \frac{Q_{CP}}{\pi(4R^2 - 4r_j^2)(2R - 2r_j)} \sim \frac{Q_{CP}}{\pi(R^2 - r_j^2)(R - r_j)} \quad (12)$$

462 The thinning of fluid neck occurs when it is stretched and elongated at high Ca_{out} . Thus, as the
 463 radius of fluid neck decreases, the shear rate of the continuous phase (i.e., CMC in our case)
 464 starts to decrease, and the viscosity of continuous phase will increase for a shear-thinning fluid.
 465 As a result, the droplet size will start to be reduced beyond a critical Ca_{out} , as shown in Fig.12
 466 when $We_{in}=0.206$. When the inner radius of the collection tube is 0.3 mm, the droplet size
 467 increases from 0.40 mm to 0.55 mm as Ca_{out} is increased from 1.5×10^{-4} to 0.0053, while the
 468 droplet size is reduced to 0.38 mm when Ca_{out} is further increased to 0.015. At a given Weber
 469 number, the droplet size first increases below a certain critical Capillary number due to the
 470 reduced viscosity, and then decreases above the critical Capillary number, when the viscosity

471 starts to increase again. The correlation between the droplet size and the Capillary number in the
472 Newtonian/shear-thinning two-phase system is different from that in the Newtonian/Newtonian
473 two-phase system, which normally shows that droplet size scales inversely with the Capillary
474 number of the continuous phase in a monotonous fashion.³⁸The different correlation highlights
475 the complex viscosity effect towards the control over emulsion droplets generated with fluid-
476 fluid systems involving shear-thinning non-Newtonian fluids. This understanding can provide
477 information needed for designing microdevices for generating droplets with well-defined
478 volumes when shear-thinning non-Newtonian multiphase systems are involved. For example,
479 given certain flow conditions and fluid properties (thus We_{in} and Ca_{out} are known), an analysis
480 can be made to determine the size of collection tube of the microdevice, according to the
481 expected size of droplets in demand.



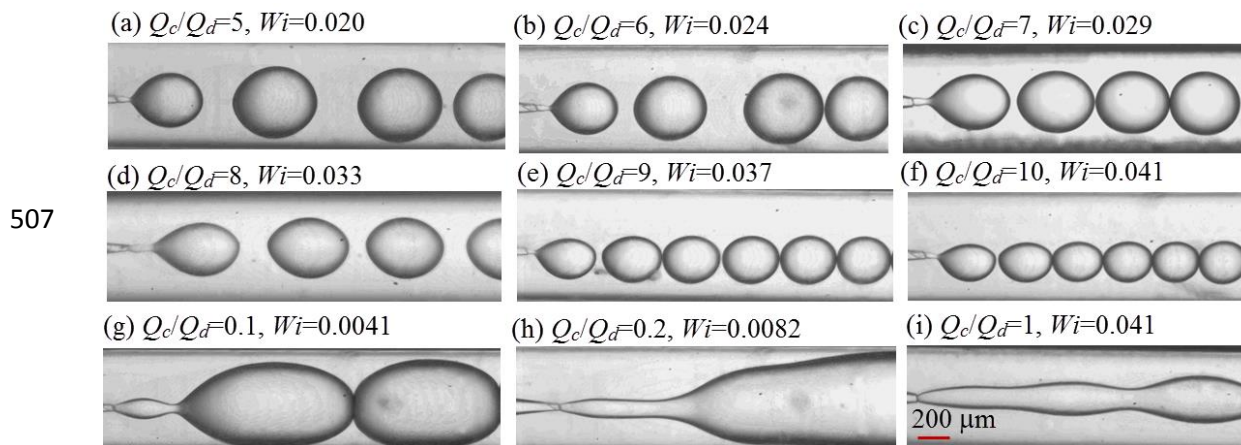
483 **Fig.12** Experimental result of droplet size as a function of the Capillary number for a given
 484 collection tube in a Newtonian/shear-thinning two-phase system (silicon oil as dispersed phase
 485 and CMC solution as continuous phase). $We_{in}=0.206$.

486 When a Newtonian liquid is surrounded by a shear-thinning liquid with pronounced elastic
 487 property, the droplet breakup dynamics gets modified. We observe flow patterns at different
 488 ratios of flow rate of 5% w/v PAA solution, which is the viscoelastic continuous phase, to that of
 489 silicon oil as dispersed phase, as shown in Fig.13. The flow rate of dispersed phase is fixed at 1
 490 ml/h in Fig.13a-f, and 10 ml/h in Fig.13g-i. The elastic forces from viscoelastic continuous phase
 491 can help to overcome interfacial tension, and thus facilitate transition to jetting at smaller

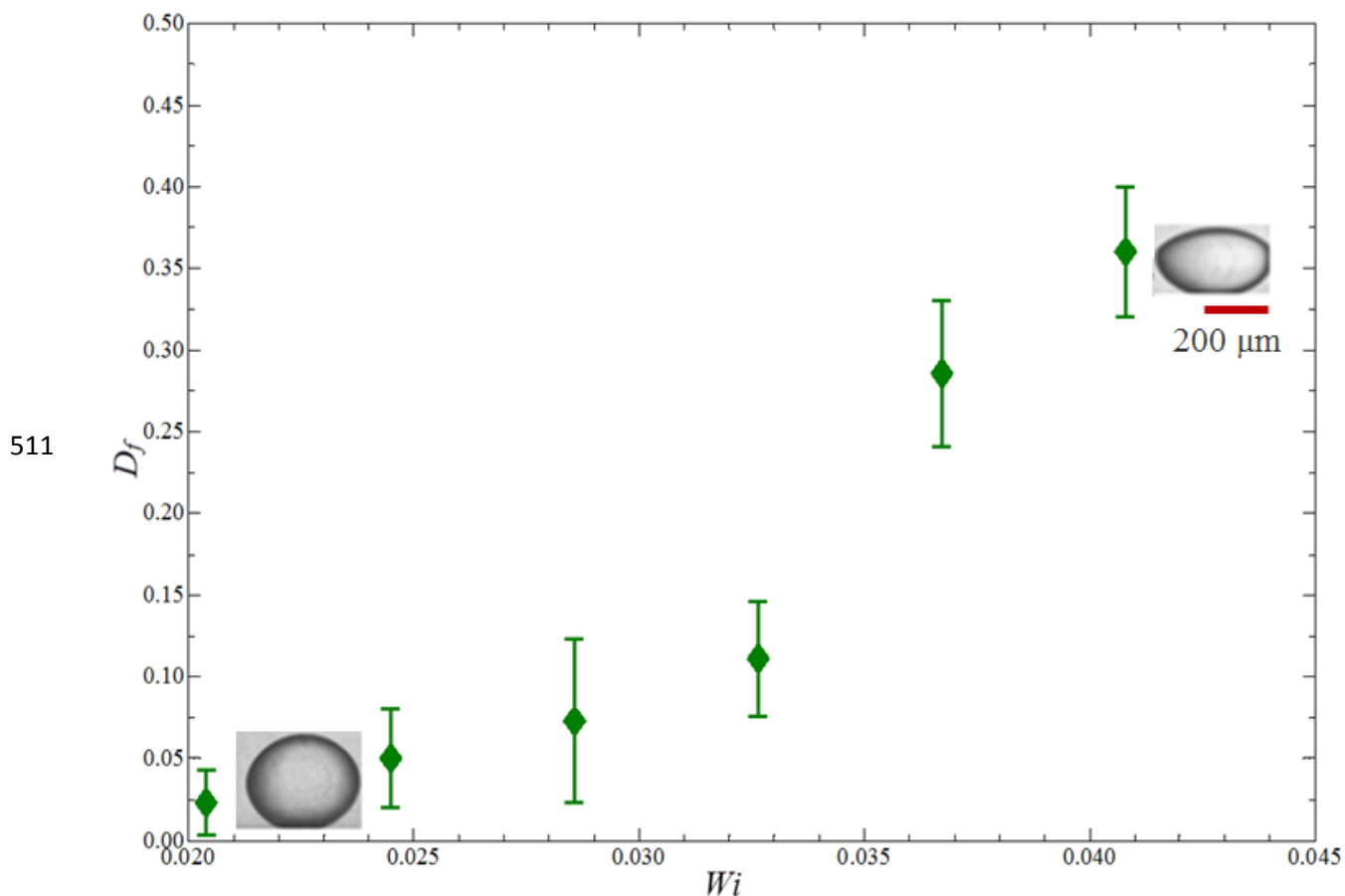
492 magnitudes of the viscous forces. Compared to the aforementioned Newtonian/Newtonian or
 493 Newtonian/shear-thinning multiphase microsystem where droplets normally adopt a spherical or
 494 nearly spherical shape, the droplets experience significant deformation in the viscoelastic non-
 495 Newtonian continuous phase. For instance, the droplets adopt an elliptical shape after breakup
 496 and relax into pointed shapes. Droplets become more pointed as the radius decreases and the
 497 flow rate ratio increases before it transitions to the jetting regime (see Fig.13a-f). The degree of
 498 droplet deformation has been characterized based on Taylor's analysis,³⁹

$$499 \quad D_f = \frac{L-W}{L+W} \quad (13)$$

500 where L is the half-length and W the half-breadth of the droplet. D_f increases with increasing
 501 Weissenberg number (thus more pronounced elastic effect), leading to formation of droplets with
 502 more pointed shape, as shown in Fig.14. This observation is consistent with the previous finding
 503 that elasticity of the suspending liquid can facilitate the deformation of the Newtonian
 504 droplets.⁴⁰ Our work provides a platform which will help to facilitate understanding of the
 505 complex rheology behavior of viscoelastic fluid and how this behavior can affect the breakup
 506 dynamics and droplet formation in multiphase microfluidic system.



508 **Fig.13** Flow patterns at selected flow rate ratios of continuous phase over dispersed phase in a
 509 Newtonian/elastic-shear-thinning two-phase system (silicon oil as dispersed phase and PAA
 510 solution as continuous phase). $Q_d=1$ ml/h for (a)-(f), and $Q_d=10$ ml/h for (g)-(i).



512 **Fig.14** Degree of deformation of droplet as a function of the Weissenberg number in a
 513 Newtonian/elastic-shear-thinning two-phase system (silicon oil as dispersed phase and PAA
 514 solution as continuous phase). The inset images show droplet adopts nearly spherical shape at
 515 low Wi , while pointed shape at high Wi , respectively. The scale bar applies for both inset images.

516 5. Conclusions

517 The work reports investigation of emulsion formation using a Newtonian/shear-thinning two-
518 phase microsystem. With a shear-thinning continuous phase, the droplet dynamics is
519 characterized to predict the dripping-to-jetting transitions under different flow conditions (as
520 function of Weber number and Capillary number), where undesirable satellite droplets may be
521 formed. Inertial effects have been shown to be important for inducing the formation of a satellite
522 droplet, while the droplet formation can be suppressed by increasing viscous effect. Due to the
523 shear-thinning characteristics of the continuous phase used in the present study, the viscosity is
524 dramatically reduced at the interface; viscous effect is therefore attenuated, leading to a faster
525 breakup and a larger droplet size. Emulsions generated with non-Newtonian fluids are routinely
526 involved in drug delivery and other biochemical applications. Accurate dosing must be ensured
527 for reliable operation, and this requires excellent control over the droplet size. We also identify
528 the correlation between the droplet size and Capillary number, potentially enabling a higher
529 degree of control over the size of emulsion droplet generated with shear-thinning fluids. Finally,
530 a viscoelastic fluid is used as continuous non-Newtonian phase, and the degree of Newtonian
531 droplet deformation increases with increasing Weissenberg number of suspending non-
532 Newtonian fluid, indicating the important impact of elasticity on the droplet shape. Our work
533 provides a first framework for understanding a range of behaviors in non-Newtonian multiphase
534 microsystems, although we recognize the vast variety of non-Newtonian fluids besides the two
535 types (shear-thinning solution with or without elastic property) we have investigated and the
536 large regions of unexplored operating conditions. For example, it is challenging to generate
537 droplets with non-Newtonian fluids in aqueous two phase systems (ATPS) due to much lower
538 interfacial tension when compared with oil-water systems.⁴¹⁻⁴² Furthermore, it is also of great
539 interest to investigate the cases when non-Newtonian fluid is used as the dispersed phase, rather

540 than just the continuous phase. Improvement in the polydispersity of the resultant droplets can
541 also be achieved potentially by developing and implementing methods to dynamically control the
542 merging of satellite droplets with the main droplets. This approach of elimination of satellite
543 droplets will also lead to droplets with higher size uniformity in applications that inevitably
544 involve non-Newtonian multiphase flows.

545 **Acknowledgement**

546 This research was supported by the Early Career Scheme (HKU 707712P) and the General
547 Research Fund (HKU 719813E) from the Research Grants Council of Hong Kong, the Young
548 Scholar's Program (NSFC51206138/E0605) from the National Natural Science Foundation of
549 China, the Basic Research Program-General Program (JC201105190878A) from the Science and
550 Technology Innovation Commission of Shenzhen Municipality, as well as the Seed Funding
551 Programme for Basic Research (201211159090) and Small Project Funding (201109176165)
552 from the University of Hong Kong.

553 **Reference**

- 554 1 H.C. Shum, D. Lee, I. Yoon, T. Kodger and D.A. Weitz, *Langmuir*, 2008, **24**, 7651–7653.
- 555 2 T. Kong, J. Wu, M.To, K.W.K. Yeung and H.C. Shum, *Biomicrofluidics*, 2012, **6**, 034104.
- 556 3 C.I. Zoldesi, P. Steegstra and A. Imhof, *J. Colloid Interface Sci.*, 2007, **308**, 121–129.
- 557 4 J.K. Nunes, S.S.H. Tsai, J. Wan and H.A. Stone, *J. Phys. D Appl. Phys.*, 2013, **46**, 114002.
- 558 5 C.H. Choi, H. Yi, S. Hwang, D.A. Weitz and C. Lee, *Lab Chip*, 2011, **11**, 1477.

- 559 6 C.M. Hwang, A. Khademhosseini, Y. Park, K. Sun and S. Lee, *Langmuir*, 2008, **24**, 6845–
560 6851.
- 561 7 J.Wu, T. Kong, K.W.K.Yeung, H.C. Shum, K.M.C. Cheung, L. Wang, and M.K.T. To, *Acta*
562 *Biomaterialia*, 2013,**9**(7), 7410-7419.
- 563 8 Ö.E. Yildırım and O.A. Basaran, *J. Non-Newtonian Fluid Mech.*, 2006, **136**, 17–37.
- 564 9 A.R. Abate, M. Kutsovsky, S. Seiffert, M. Windbergs, L.F.V. Pinto, A.Rotem, A.S. Utada and
565 D.A. Weitz, *Adv. Mater.*, 2011, **23**, 1757–1760.
- 566 10 C. L. A. Berli, *J. Colloid Interface Sci.*, 2010, **349**, 446–448.
- 567 11 T. Nguyen, Y. Xie, L. J. de Vreede, A. van den Berg and J.C.T. Eijkel, *16th Int. Conf. on*
568 *Miniaturized Systems for Chemistry and Life Sciences*, 2012, 1987–1989.
- 569 12 D.J. McClements, *Crit. Rev. Food Sci.Nutr.*, 2007, **47**, 611–649.
- 570 13 A. Budhian, S.J. Siegel and K.I. Winey, *Int. J. Pharm.*, 2007, **336**, 367–75.
- 571 14 C. Berkland, M. King, A. Cox, K. Kim and D. Pack, *J. Control Release*, 2002, **82**, 137–47.
- 572 15 R.M. Erb, D. Obrist, P.W. Chen, J. Studer and A.R. Studart, *Soft Matter*, 2011, **7**, 8757.
- 573 16 M.S.N. Oliveira and G.H. McKinley, *Phys. Fluids*, 2005, **17**, 071704.
- 574 17 J. Eggers¹ and E. Villermaux, *Rep. Prog. Phys.*, 2008, **71**, 036601.
- 575 18 A.S. Utada, A. Fernandez-Nieves, H.A. Stone and D.A. Weitz, *Phys. Rev. Lett.*, 2007, **99**,
576 094502.
- 577 19 R.G.Larson, *The structure and rheology of complex fluids*, Oxford University Press, Oxford,
578 1999.
- 579 20 S. Yang, J.Y. Kim, S.J. Lee, S.S. Lee, and J.M. Kim, *Lab Chip*, 2011, **11**, 266.
- 580 21 L. Derzsi, M. Kasprzyk, J.P. Plog, and P. Garstecki, *Phys. Fluids*, 2013, **25**, 092001.
- 581 22 G. Pangalos, J.M. Dealy and M.B. Lyne, *J. Rheol.*, 1985, **29**, 471–491.

- 582 23 A. Sauret, C. Spandagos and H.C. Shum, *Lab Chip*, 2012, **12**, 3380.
- 583 24 L.Sang, Y.Hong and F. Wang, *Microfluid Nanofluid*, 2009,**6**, 621–635.
- 584 25 C.L. Tucker, *Hanser Publishers*, New York, 1989.
- 585 26 Y. Hong and F. Wang, *Microfluid Nanofluid*, 2007, **3**,341–346.
- 586 27 A. Benchabane and K. Bekkour, *Colloid. Polym. Sci.*, 2008, **286** (10), 1173-1180.
- 587 28 K. Benyounes, *13th SGEM GeoConference on Science and Technologies In Geology,*
588 *Exploration and Mining*, 2013, 951–95.
- 589 29 S.M.F.D. Syed Mustapha, T.N. Phillips, C.J. Price, L.G. Moseley and T.E.R. Jones, *Eng. Appl.*
590 *Art. Intell.*, 1999, **12**, 255.
- 591 30 S.D. Geschiere, I.Ziemecka, V. van Steijn, G.J.M. Koper, J.H. van Esch and M.T. Kreutzer,
592 *Biomicrofluidics*, 2012,**6**, 022007.
- 593 31 A. Kreiba, *The Rheological Properties of Aqueous Polyacrylamide Solutions*, Concordia
594 University, 2000.
- 595 32 R. G. Larson, *Constitutive Equation for Polymer Melts and Solutions*, Butterworth-
596 Heinemann, 1988.
- 597 33 J. Eggers, *ZAMM ·Z. Angew.Math. Mech.*, 2005, **85**,400–410.
- 598 34 M.Rohani, F.Jabbari and D. Dunn-Rankin, *Phys. Fluids*, 2010, **22**, 107103.
- 599 35 M. Tjahjadi, H.A. Stone and J. M. Ottino, *J. Fluid Mech.*,1992, **243**,297–317.
- 600 36 G.I. Taylor, *Proc. R. Soc.LondonSer.A*, 1932, **138**, 41–47.
- 601 37 H. Song, D.L. Chen and R.F.Ismagilov, *Angew. Chem. Int. Ed.*, 2006, **45**, 7336–7356.
- 602
- 603 38 C.A. Stan, S.K.Y. Tang and G.M. Whitesides, *Anal. Chem.*, 2009, **81**, 2399–2402.
- 604 39 G.I. Taylor, *Proc. Roy.Soc.A*, 146 (1934) **501**.

605 40 D.C. Tretheway and L.G. Leal, *J. Non-Newtonian Fluid Mech.*, 2001, **99**, 81–108.

606 41 Y.Song, A. Sauret and H.C. Shum, *Biomicrofluidics*, 2013,**7**, 061301.

607 42 A.Sauret and H.C. Shum, *Appl. Phys. Lett.*,2013, **100**, 154106.